Late Pleistocene – Holocene denudation, uplift, and morphology evolution of the Armorican Massif (western Europe)

Oswald Malcles~~, O.~~ [1]~~,~~, Stéphane Mazzotti ~~S.~~ [2]~~,~~, ~~-~~Philippe Vernant ~~P.~~ [3], Vincent Godard~~ V.~~ [4]

[1] Institut des Sciences de la Terre. Université Savoie-Mont-Blanc, Université Grenoble Alpes, Centre National de la Recherche Scientifique, Institut de Rercherche pour le Développement, Université Gustave Eiffel. 24-28 Avenue du Lac d'Annecy, 73370 Le Bourget-du-Lac, France.

[2] Laboratoire de Planétologie et Géosciences. Université de Nantes, Centre National de la Recherche Scientifique, Université d'Angers, Université du Mans. 2 Chemin de la Houssinière Bâtiment 4, 44300 Nantes, France.

[3] Géosciences Montpellier. Université de Montpellier, Centre National de la Recherche Scientifique. Place Eugène Bataillon, 34090 Montpellier, France

[4] Centre Européen de Recherche et d'Enseignement des Géosciences de l'Environnement. Aix Marseille Université, Centre National de la Recherche Scientifique, Institut de Rercherche pour le Développement, Institut national de recherche pour l'agriculture, l'alimentation et l'environnement. Technopôle de l'Arbois-Méditerranée, BP80, 13545 Aix-en-Provence, France~~1. ISTerre, Université Savoie-Mont-Blanc, Université Grenoble Alpes, CNRS, IRD, Université Gustave Eiffel~~

~~[2] Laboratoire de Planétologie et Géosciences, Université de Nantes, CNRS, Université d'Angers, Université du Mans~~

~~[3]. *Géosciences Montpellier, Université de Montpellier, CNRS*~~

~~[4]. *Aix Marseille Univ, CNRS, IRD, INRAE, CEREGE, Aix-en-Provence, France*~~

Correspondence to: Oswald Malcles (oswald.malcles@univ-smb.fr)

Abstract

Elevated Plio-Pleistocene coastal and marine markers in stable continental regions are commonly explained by a combination of eustatic sea-level variations and large-scale geological processes (e.g., crustal or mantle dynamics). In this study, we test the role of erosion rates on the Late Pleistocene uplift and landform evolution of the Armorican Massif, western France. Denudation rates

are estimated for 19 drainage basins using terrestrial cosmogenic nuclide (^{10}Be) measurements in quartz. They range between 3 and 27 m.Ma^{-1}, with a factor of two difference between the western highland region and the central lowland region (13 ± 6 m.Ma^{-1} vs. 7 ± 4 m.Ma^{-1}). Assuming a thin elastic plate model, the lithosphere flexural isostatic response to these denudation rates produces an overall uplift rate of the Armorican Peninsula from 12–15 m.Ma^{-1} in the central lowland region to 4–10 m.Ma^{-1} in the western peninsula and along the coastline. We show that these erosion-driven uplift rates can explain the uplifted Late Pleistocene marine terraces along the Armorican Peninsula coastline as well as the elevated Quaternary marine deposits in the central lowland region, without necessitating additional geodynamic processes such as regional compression or local active faults. Our results suggest that, in stable continental regions, long-term erosion should be taken into account as a driver of uplift and deformation before trying to derive global or regional geodynamic or tectonic conclusions.

1. Introduction

Plio-Pleistocene uplift rates ca. 10 – 100 m·Ma^{-1} are observed in numerous stable continental regions, i.e., in areas unaffected by direct plate-boundary processes (e.g., Australia, South Africa, northwestern Europe). Most of these uplift rates are derived from elevated coastal or alluvial landforms, such as marine terraces, planation surfaces (rasas) or river terraces, and from sedimentary records, such as raised beaches or endo-karstic infilling. The origins of these slow coastal uplift rates are debated (e.g., Erlanger et al., 2012) and have been attributed to a large variety of geodynamic processes: global mantle dynamics (Gurnis et al., 2000) or plate tectonics (Pedoja et al., 2011), regional lower crustal flow triggered by glaciation cycles (Westaway et al., 2002), local fault reactivation (Bonnet et al., 2000), or local volcanism (Murray-Wallace et al., 1996). Surprisingly, none of these studies consider the role of long-term erosion as a potential driver of coastal uplift through simple isostatic adjustment.

Here, we address the relationship between long-term erosion rates, uplift rates, and landform evolution of the Armorican Massif, western France (Fig. 1) during the Late Pleistocene – Holocene epochs. This region comprises several coastal landforms and marine deposits that witness recent uplift of the whole area, including indications of spatial uplift variations that may reflect local fault reactivation (cf. Section 2). In addition to numerous uplift rate data, the Armorican Massif offers several specific advantages for testing the role of erosion in local and regional uplift: Due to its geography, the impact of the mass removal from the studied area is almost isolated from other mass-modification origins. No onshore mass transfer is indeed possible from the neighboring regions ~~peculiar geography, it is only affected by local erosion. Mass redistribution from regional inland sources is not possible~~ due to the radial-like structure of the hydrographical network. All the eroded material is either stocked locally or exported to the sea. The offshore areas, associated with mass-modifications in the long term are, either located far enough from the shore line (continental talus) or are associated with low deposit rates over ~~watershed geometry, and offshore processes (e.g., talus deposits) are negligible due to their low~~ the long-term (continental plateau, cf. section~~magnitudes (cf. Section~~ 4). This provides a low-to-negligible impact due to offshore mass redistribution. This assumption is tested in section 4.

The massif erosion pattern can be estimated by quantifying erosion rates at a spatial scale of a few tens of kilometers owing to the relatively small watersheds ~~based on small watershed sampling,~~ while keeping rather homogeneous ~~homogenous~~ morphology (Fig. 2), lithology, or climates, hence production rates and processes acting on the morphogenesis ~~production rates, etc.~~. Finally, its geology consists primarily of quartz-rich basement and metasediment formations, which allow for estimations of denudation rates at the scale of drainage basins using terrestrial cosmogenic nuclide (^{10}Be) measurements in quartz.

In the following, after a short description of the regional geological and geomorphological setting and evolution, we detail the sampling strategy and processing methodology to derive new denudation rates in 19 watersheds covering the Armorican Massif. These new data are then integrated within a regional Western European database to construct denudation rate models for the whole Armorican Massif and neighboring areas, which then serve as inputs for models of uplift rates driven by flexural isostatic adjustment. Given the magnitudes and uncertainties in denudation rates, apparent uplift rates, and eustatic sea level corrections, our analyses show that Pleistocene–Holocene absolute uplift rates in the Armorican Massif can be explained by the flexural isostatic response to local denudation rates (at wavelengths of 50–100 km), without need for additional processes such as lithosphere bulging or local fault activity. Additional processes cannot be ruled out but, if present, must be significantly slower than previously proposed.

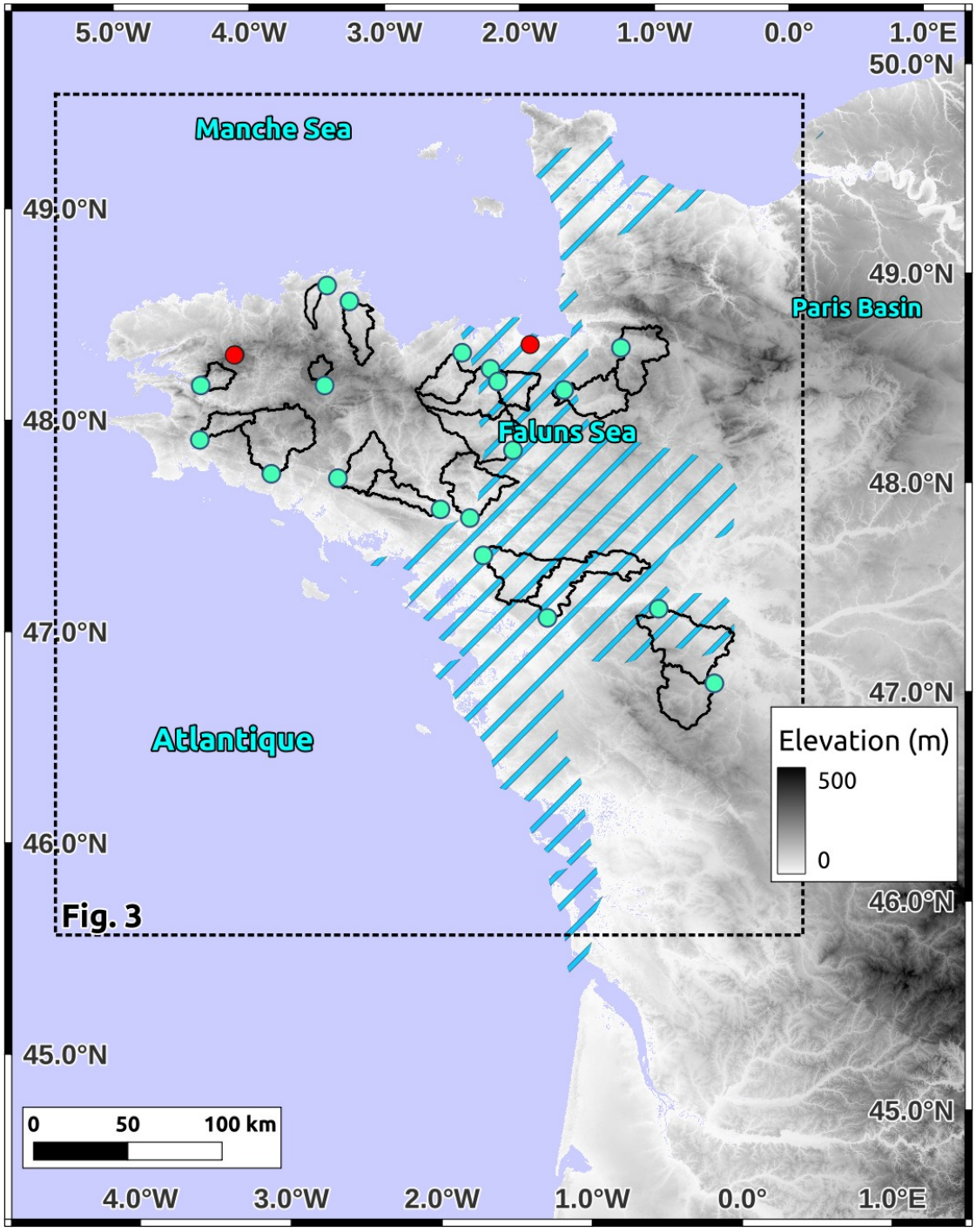

70 **Figure 1. Armorican Massif topographic map. DEM from JAXA-ALOS W3D30. The studied watersheds are delimited by the black-contoured polygons with the sampling sites identified with the blue points. Outcrop sampling sites are marked by the red points. Blue stripes: approximate onshore extent of the Mio-Pliocene "Faluns Sea" (Néraudeau et al., 2010).**

2. Geological and geomorphological setting

The Armorican Massif, western France, corresponds mostly to the remnant basement and structures of the Cadomian (650–540 Ma) and Variscan (370–300 Ma) orogens (Ballèvre et al., 2009). It comprises four main tectonic domains separated by major crustal-scale faults and shear zones (North-Armorican and South-Armorican Shear Zone systems), with other major fault systems also noticeable (e.g., Quessnoy-Nort-sur-Erdre Fault, QNEF, Fig. 2~~3~~). Its Meso-Cenozoic geological history is marked by minor fault reactivations associated with far-field tectonic events (e.g., North Atlantic Ocean opening, Pyrenean orogeny~~, ...~~), up to the present-day moderate background seismicity indicating small ongoing deformation (Beucler et al., 2021). Overall, the Armorican Massif is primarily composed of Proterozoic and Paleozoic crystalline basement and metasediment formations, with limited remnants of Meso-Cenozoic sedimentary deposits. Studies of planation surfaces and stratigraphic constraints indicate at least two major phases of burial and exhumation during the mid-Mesozoic and the late-Cretaceous – early-Eocene (Bessin et al., 2014). The thicknesses of the associated sedimentary covers (and thus the eroded thicknesses) are poorly constrained but were probably limited to several hundred meters, based on the remaining deposits. Several later episodes of minor marine transgressions and sediment deposits occurred during the Cenozoic, up to the most recent Red Sands and Faluns associated with the "Faluns Sea" (Fig. 1) during the Upper Miocene – Pliocene (Guillocheau et al., 2003).

These Red Sands and Faluns formations correspond to two cycles of marine transgressions / regressions during the Upper Miocene (5–8 Ma) and the Upper Pliocene (2–3 Ma), with marine flooding limited to the present-day low-elevation regions of central Brittany and Normandy (Fig. 1). While the Faluns deposits are good markers for estimations of long-term uplift rates owing to their shallow-depth open-marine fauna, the Red Sands provide less robust uplift markers due to their complex nature of continental sheetflood, fluvial, and estuarine deposits (Néraudeau et al., 2003; Brault et al., 2004). Their sedimentary and stratigraphic characteristics point to a system of shallow-water marine transgressions between elevated continental domains, with an overall smooth topography and large braided rivers directly connected to numerous estuaries (Guillocheau et al., 2003; Brault et al., 2004). They also indicate a relatively high clastic discharge from two continental domains on both sides of the main north-south divide (i.e., "West Armorican and North Cotentin islands" scenario). This Mio-Pliocene configuration changes during the Mid Pleistocene (ca. 1–1.5 Ma), with the disappearance of marine deposits and the formation of the present-day drainage network that incises into the Red Sands and Faluns formations. In contrast with the Mio-Pliocene system, the current (Pleistocene – Holocene) drainage network is characterized by incised valleys and jagged topography with a main east-west divide. The rivers tend to be spatially associated with tectonic scarps and structures (e.g., following the major NW-SE exhumed shear zones in southern Britany), indicating either differential erosion along weaker inherited faults and shear zones, or a control by a potential recent reactivation of these structures (Bonnet et al., 1998, 2000).

These various Cenozoic marine deposits and landforms provide detailed information on the topographic evolution of different sectors of the Armorican Massif. Hereafter, we refer to "apparent uplift" when considering the elevation of paleo

marine markers relative the present-day sea level due to a combination of eustatic sea level variation and vertical land movement, in contrast with “uplift” which is used to refer to vertical land motion (i.e., corrected for eustatic variations).

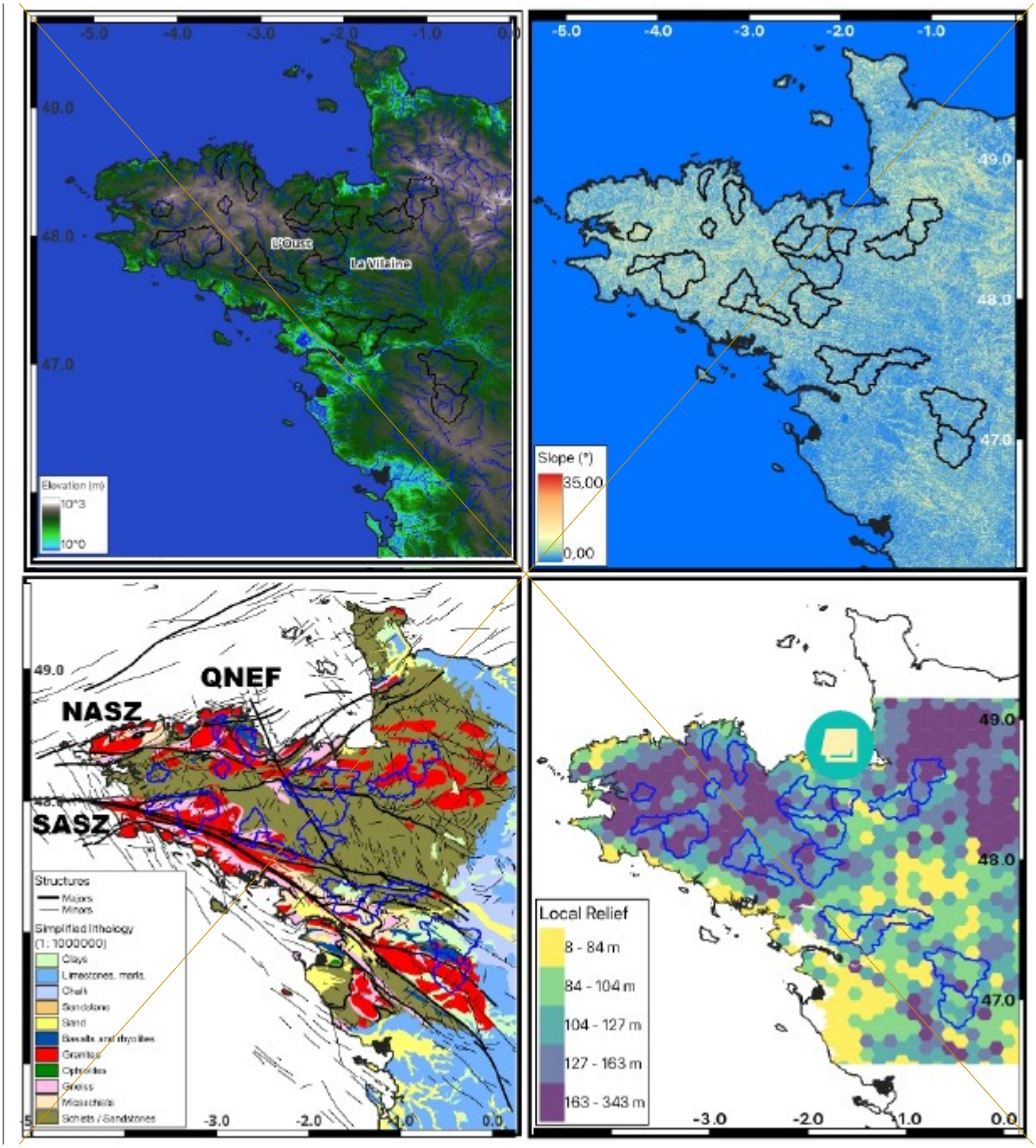

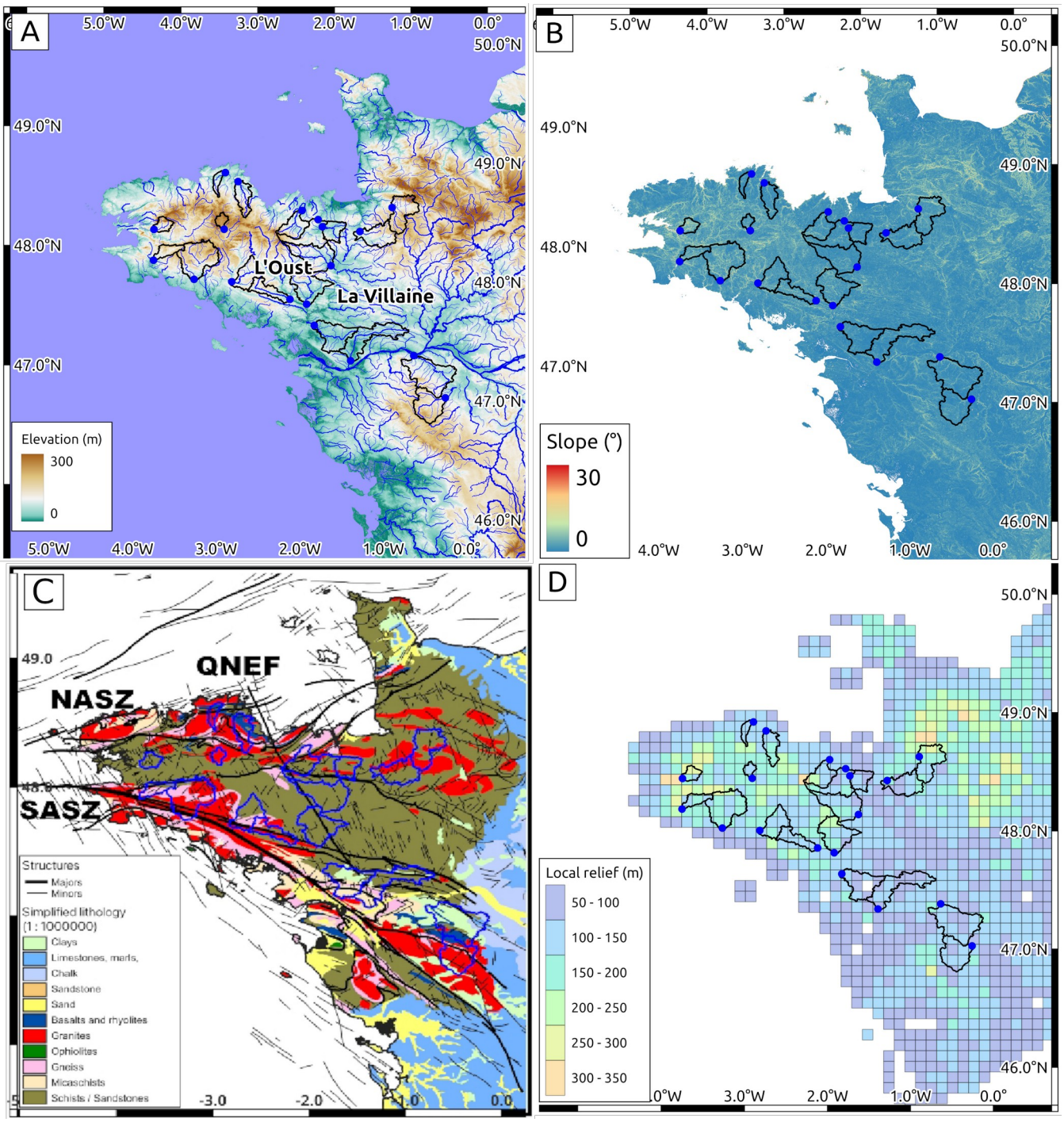

110

Figure 2: Top left: Elevation map in a log10 scale to highlight the regional pattern (DEM data from JAXA, river network from ©OpenStreetMap, Distributed under the Open Data Commons Open Database License (ODbL) v1.0. The two main basins (Oust and Vilaine) are located. Top right: slope map of the studied area. Bottom left: Simplified geological map (wms data from BRGM:

~~http://geoservices.brgm.fr/geologie). Main tectonic structures shown in black (SASZ: South Armorican Shear Zone; NASZ: North Armorican Shear Zone; QNEF: Quessoy-Nort-sur-Erdre Fault). Bottom right: relief calculated for the 100 km2 hexagonal grid.~~

Figure 2: A: Elevation map (DEM data from JAXA), river network from ©IGN. The two main basins (Oust and Vilaine) are located. B: slope map of the studied area. C : Simplified geological map (wms data from BRGM: http://geoservices.brgm.fr/geologie). Main tectonic structures shown in black (SASZ: South Armorican Shear Zone; NASZ: North Armorican Shear Zone; QNEF: Quessoy-Nort-sur-Erdre Fault). D: relief calculated for the 100 km2 rectangular grid.

The marine Mio-Pliocene Faluns are found at present-day elevations between ca. 20 and 90 m. Assuming a eustatic sea level highstand of 60 m during the Upper Pliocene (relative to present-day sea level) and based on ESR (Electron Spin Resonance) dating, Brault et al. (2004) estimate an uplift of 12–40 m of the second maximum flooding surface situated in the central low-elevation region of the Armorican Massif. This would correspond to an average uplift rate in this area of 4–13 $m \cdot Ma^{-1}$ since ca. 3 Ma. This estimation is in rough agreement with those by Bessin et al. (2017) based on a reanalysis of marine deposits and sea-level curves, which yield average Pleistocene uplift rates of 16 ± 2 and 29 ± 2 $m \cdot Ma^{-1}$ for the low-elevation regions of Britany and Normandy. No uplift estimations exist for the high- elevation domains.

More recent estimations can be derived from the numerous Pleistocene marine terraces and rasas (wave-cut platform) that mark the coastline of Brittany and Normandy. Using the compilation of Pedoja et al. (2018), we estimate an average apparent uplift since MIS 5e (last interglacial, ca. 130 ka) of 6 m for western Brittany (31 terraces), 5 m for western Cotentin (7 terraces), and 8 m for the Channel Islands (4 terraces). These values are associated with an accuracy of 1–3 m based on the margin of error defined in Pedoja et al. (2018) and on the data standard deviations. The eustatic sea level highstand during MIS 5e was located between ca. 3 m (Siddall et al., 2007) and ca. 7.5 m (Dutton and Lambeck, 2012) above present-day sea level, leading to an uplift between -1.5 m and 3 m for western Brittany, -2.5 m and 2 m for western Cotentin, and 0.5 m and 5 m for the Channel Islands (negative uplift values indicate subsidence). Thus, the Late Pleistocene regional trend may correspond to a period of slow uplift rate (15–40 $m \cdot Ma^{-1}$) assuming a low eustatic highstand of 3 m, or a period of slow subsidence rate (-20–0 $m \cdot Ma^{-1}$) for a high eustatic highstand of 7.5 m. For the penultimate interglacial (MIS 11, ca. 400 ka), Pedoja et al. (2018) estimate an average apparent uplift of 20 m of western Europe marine terraces and rasas. Combined with a eustatic sea level highstand of 6–13 m (Muhs et al., 2012; Raymo and Mitrovica, 2012), this yields an average uplift rate of 18–35 $m \cdot Ma^{-1}$ since 400 ka. A few studies provide information on recent relative or absolute uplift rates in the Armorican Massif.

Geomorphic analyses of river incisions and watershed morphologies indicate a differential uplift of ca. 30 m between western Britany (Oust watershed) and central Britany (Vilaine watershed) (Bonnet et al., 1998). A similar differential uplift of western Britany relative to the central low-elevation area is deduced from numerical analyses of the topography and slope / drainage relationships (Lague et al., 2000). Assuming that this morphological difference is inherited from a differential uplift since the Pleistocene, these studies indicate a relative west / center uplift rate of ca. 10–15 $m \cdot Ma^{-1}$. Bonnet et al. (1998) propose a faster relative rate of 40–60 $m \cdot Ma^{-1}$ based on archeological finds in one terrace on the northern coastline of the Oust watershed (lithic industry from the Cromerian stage, 0.7–0.5 Ma , Monnier et al., 1981). The leveling data analysis of Lenôtre et al. (1999)

supports the relative west vs. center uplift, albeit at a differential rate of 1000 m·Ma^{-1} (1 mm·a^{-1}) or more. Recent results using GNSS (Global Navigation Satellite System) data show that this differential rate is likely overestimated, due to biases inherent to
150 old leveling data, and that present-day vertical rates in the Armorican Massif are below the resolution of geodetic data, i.e., lower than ca. 500 m·Ma^{-1} (0.5 mm·a^{-1}) (Masson et al., 2019).

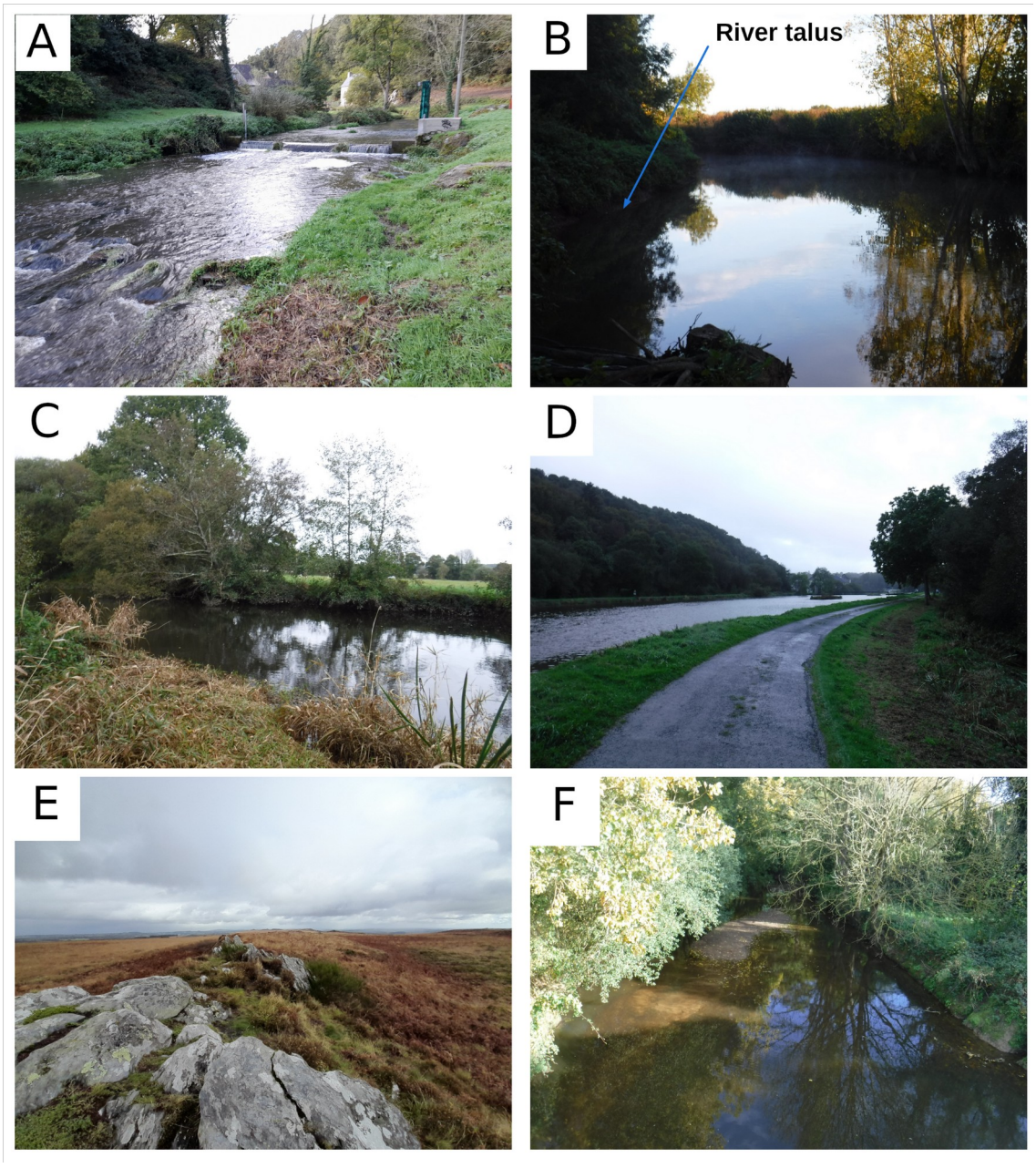

Figure 3: Photography of common landscape and sampling site types. A- Guindy river sampling site. Example of small scale anthropic disturbances. B- Meu river sampling site, view toward upstream. Example of surrounding flat topography with local river talus and generalized tree-covered flanks. C- Claie river sampling site. Another example of surrounding flat topography with local river talus and crops/bocage landscape. D- Example of localized relief, southern Brittany. E- Roc'h-Ruiz: example of sampled outcropping rocks and shrub-land areas. F- Arguenon sample site. View toward downstream, example sampled central sand-bar. Photos: O. Malcles

Table 1. Armorican Massif TCN denudation rates and morphology parameters

Name	Type	Area (km^2)	Mean altitude (m)	Mean slope (°)	Hypsometric Integral	Mass Quartz (g)	$^{10}Be/^{9}Be$ (x10-13)		^{10}Be (10^5 atm.g-1)		Denudation ($m \cdot Ma^{-1}$)	
							Ratio	Error	Conc.	Error	Rate	Error
Watersheds												
(1) Aff	Sand	712	78	2.6	0.39	18.429	1.14	0.04	3.77	0.15	9.5	0.9
(2) Argenton	Sand	651	155	1.8	0.51	28.973	3.59	0.13	7.77	0.31	4.6	0.4
(2) Argenton	Sand					29.852	2.00	0.09	0.42	0.22	9.1	0.9
(3) Arguenon	Sand	416	98	2.5	0.28	18.535	7.68	0.07	2.56	0.26	14.7	1.9
(4) Blavet	Sand	112	254	2.8	0.67	31.654	1.14	0.09	2.18	0.18	20.2	2.3
(5) Claie	Sand	353	97	2.8	0.52	29.535	1.43	0.06	3.03	0.15	12.2	1.2
(6) Couesnon	Sand	558	113	2.3	0.41	29.669	1.95	0.08	4.11	0.20	9.0	0.9
(7) Douffine	Sand	173	155	5.0	0.41	30.371	0.59	0.09	1.23	0.19	33.6	6.0
(7) Douffine	Cobbles					29.465	1.47	0.09	3.12	0.21	12.5	1.3
(8) Erdre	Sand	829	44	1.7	0.42	33.466	3.30	0.10	9.32	0.33	3.4	0.3
(8) Erdre	Cobbles					20.561	1.70	0.05	5.19	0.18	6.5	0.6
(9) Evel	Sand	473	105	2.6	0.51	21.101	0.89	0.07	6.18	0.22	5.7	0.5

10

(9) Evel	Cobbles					31.191	4.62	0.14	2.64	0.21	14.3	1.6
(10) Guindy	Sand	129	82	1.8	0.25	18.734	0.59	0.04	1.96	0.13	19.3	2.0
(11) Isac	Sand	681	42	1.5	0.42	20.030	0.52	0.02	1.59	0.07	22.9	2.1
(12) Laita	Sand	935	152	3.3	0.47	17.256	0.59	0.05	2.15	0.18	18.6	2.2
(13) Layon	Sand	1057	93	1.7	0.39	29.610	1.61	0.08	3.40	0.19	10.7	1.1
(13) Layon	Sand					31.325	1.74	0.07	3.51	0.16	10.3	1.0
(14) Leff	Sand	345	114	1.9	0.39	20.072	0.92	0.03	2.82	0.11	13.6	1.2
(14) Leff	Sand					17.809	0.87	0.03	3.04	0.12	12.5	1.1
(15) Linon	Sand	306	67	1.8	0.32	34.370	3.20	0.11	5.85	0.24	5.8	0.5
(16) Meu	Sand	764	90	1.9	0.34	17.852	2.29	0.07	7.84	0.26	4.3	0.4
(17) Odet	Sand	224	145	3.5	0.49	17.418	0.99	0.06	3.44	0.23	11.2	1.2
(18) Rance	Sand	894	87	2.0	0.27	24.13	0.66	0.03	1.63	0.09	23.5	2.3
(19) Selune	Sand	625	166	2.8	0.36	33.020	2.10	0.16	3.95	0.31	9.9	1.1
Outcrops												
Mont Dol	Rock	-	5	-	-	26.659	8.18	0.14	19.27	0.55	2.4	0.2
Roch'Tredudon	Vein	-	377	-	-	30.534	4.25	0.14	6.62	0.20	6.5	0.6
Roch'Tredudon	Vein	-	369	-	-	19.134	2.04	0.05	8.70	0.34	4.8	0.4

~~*Name: Watershed or outcrop location name (Fig. 2). All watershed samples are river sands, unless marked (c) for gravel to cobbles sizes. HI: hypsometric integral. Mass Qz: mass of dissolved quartz, weighted at 10 -4 g precision. The 9Be spike mass added was 150 ± 2 mL with a concentration of 3025 µg g-1. Provided ratio are blank corrected (mean of 5 blanks = 2.21 ± 0.52 E-15. C and σc: 10 Be concentration and standard error. d and σd: denudation rate and standard error.*~~

3. Denudation rates from terrestrial cosmogenic nuclide

3.1. Drainage basin sampling and 10Be measurements

To estimate denudation rates at the scale of drainage basins, we sampled quartz-rich river sands (plus threea few gravel-to-cobble samples) and measured their concentrations ofin cosmogenic beryllium 10 (^{10}Be), which is produced in quartz grains within the first few meters ofbelow the surface. This concentration is a function of the local surface production and denudation rates (e.g. Granger et al., 1996, Von Blanckenburg, 2005). Thus, ^{10}Be measurements in river sands provide an estimation of the mean upstream denudation rate above the sampling point, as long as the main hypotheses of this method are respected (e.g., nearly homogeneous quartz content in the watershed). We collected samples in exposed sand pockets along riverbanks and on sand bars, avoiding as much as possible accumulation spots due to anthropic structures and alterations of the river channel. This constraint, and the fact that downstream river sections close to the coast are often filled with mud, limited our sampling to upstream sites. In total, we sampled 19 watersheds (Table 1, Fig. 1, 2, 3), three of which were sampled twice (a few meters apart) to estimate the repeatability between sand samples (Argenton, Layon, Leff). Three others were sampled with both sands and gravel-to-cobble sediment for comparison (Erdre, Douffine, Evel).

The sand and coarser samples followed a standard preparation procedure via crushing, sieving (retaining of the 250–1000 µm fraction), leaching with HCl + HNO_3 acids, magnetic separation, suppression of non-quartz grains using multiple H_2SiF_6 baths, and final removal of the atmospheric ^{10}Be by multiple HF etchings. From the purified quartz, Be was separated following Ruszkiczay-Rüdiger et al. (2021) via multiple ion exchange chromatography and selective pH precipitation following total dissolution and the addition of 2150 +/-± 2 mµL of known ^{9}Be concentration solution with a concentration of 3025 µg g^{-1}. Measured ratios are blank corrected (mean of 5 blanks = 2.21 ± 0.52 10^{-15}). After separation, Be was oxidized at 800 °C and mixed with Nb (volumetric ratio ~ 1:1) prior to measurement. The ^{10}Be/ ^{9}Be concentration ratio was measured by accelerator mass spectrometry at the ASTER national facility AMS national facility in Aix-en-Provence , France (Arnold et al., 2010). The ratios were calibrated using ASTER standards (Braucher et al., 2015) to derive ^{10}Be concentrations.

^{10}Be concentrations in three outcrop samples were measured following the same procedure. These three sites (Fig. 3E, Fig. 4b) are located at the top of locally prominent monadnocks (no topographic mask) and are therefore expected to provide lower-bound erosion rates (i.e., rates mostly controlled by local weathering processes, with little influence of longer wavelength slope-dependent hillslope or fluvial processes). The estimated erosion rate for the outcrops are considered as being at steady-state (hence considering an “infinite exposure”, and providing a maximal denudation rate) as there is no evidence on the field for other surface evolutions such as abrupt exposure or partial burial. The samples were taken using a chisel and sledge hammer, taking samples a few centimeters thick. Drainage-basin average denudation rates were derived from ^{10}Be concentrations (see supplementary materials) using the online CRONUS-Earth system (Balco et al., 2008) (https://hess.ess.washington.edu/https://hess.ess.washington.edu/). We hereby provide the denudation rates outputs using a sea-level high-latitude ^{10}Be production rate of 4.11 ± 0.19 at.g $^{-1}$.yr^{-1} and the Stone scaling scheme (Stone, 2000) which does not take into account variations in the earth magnetic field. The use of other scaling models including this time-variation would lead to higher denudation rates of the order of 3 %. -The CRONUS-Earthis commonly-used calculator comprises some simplifications and assumptions that we consider reasonable given our study context. Some are stated here, while a more comprehensive view can be found in Balco et al. (2008) or Dunai (2010) for instance. A-mongst the common TCN hypothesis as a constant flux of

cosmic particles from extra-solar origins or an independence of the attenuation length with elevation or latitude variations. It is also assumed that steady state was achieved for the TCN concentration in the sampled material. Application of this model is expected to hold as long as the geomorphological evolution is in agreement with a simple model where e.g., denudation rates are at ~~at~~ steady-state providing a constant sand-like granulometry sediment supply with fast transport through the river network. In other words, ~~(~~no catastrophic events such as landslides~~events as landslides~~ providing deep-seated material to the river network is known, and the sediment sources are considered as being free of ~~) with river sediments without a~~ complex history including burial in river terraces for instance.~~following initial exposure (no significant burial in river terraces)~~ The model also uses a single muon attenuation length and assumes a constant density throughout the entire eroded column. We use the ~~;~~ mean watershed slope and latitude are used for computation of the production rate scaling factor. Given the regional morphology (small elevation span), the homogeneous climate, and the small size of the sampled watersheds, we consider that adding more complexity in our denudation rate estimations (e.g., spatial and temporal evolution of the tree cover) is not required.

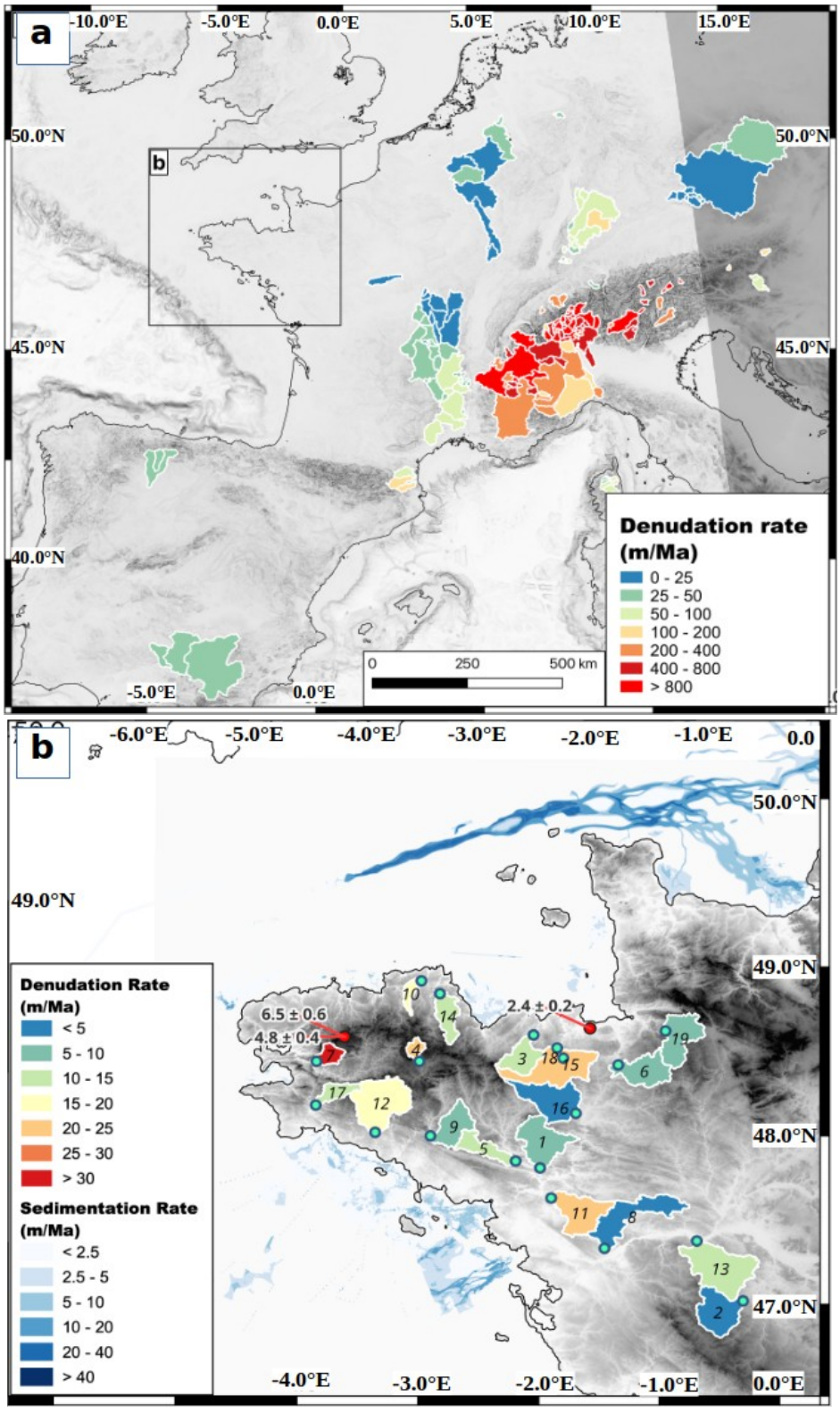
a
-10.0°E
-5.0°E
0.0°E
5.0°E
10.0°E
15.0°E
50.0°N
45.0°N
40.0°N
b
Denudation rate
(m/Ma)
0 - 25
25 - 50
50 - 100
100 - 200
200 - 400
400 - 800
> 800
0
250
500 km
b
-6.0°E
-5.0°E
-4.0°E
-3.0°E
-2.0°E
-1.0°E
0.0
50.0°N
49.0°N
48.0°N
47.0°N
Denudation Rate
(m/Ma)
< 5
5 - 10
10 - 15
15 - 20
20 - 25
25 - 30
> 30
Sedimentation Rate
(m/Ma)
< 2.5
2.5 - 5
5 - 10
10 - 20
20 - 40
> 40
6.5 ± 0.6
4.8 ± 0.4
2.4 ± 0.2
1
2
3
4
5
6
7
8
9
10
11
12
13
14
15
16
17
18
19

Figure 4. Drainage basin data used in the denudation rate model. A) Data from the Octopus drainage basin denudation database (Codilean et al., 2018) used for synthetic denudation rate modeling. B) Armorican Massif data from this study. Blue dots: sampling locations of drainage basin, with basin number in each polygon (see table 1). Red dots: sampling locations of outcrops with estimated denudation rate. Quaternary sedimentation rates around the Armorican Peninsula from Augris et al. (2013c, a, b).

3.2. Denudation rates

The denudation rates measured in the 19 drainage basins of the Armorican Massif (Table 1) vary between 3 and 27 m.Ma^{-1}, for an average rate of 10 ± 6 m.Ma $^{-1}$ (mean ± standard deviation). ~~Assuming a sea-level high-latitude 10 Be production rate of 4.11 ± 0.19 at.g -1.yr-1 and the Stone scaling scheme (Stone, 2000),~~ T~~ t~~hese denudation rates are associated with an integration time between ca. 20 kyr and 200 kyr (average 45 kyr) (Von Blanckenburg, 2005). Thus, they are representative of the Late Pleistocene period but are also sensitive to the Late Pleistocene - Holocene climate transition and its impact on denudation rates (e.g., Schaller et al., 2002). Because of the integration times, we consider that our rates are mostly indicative of Late Pleistocene average conditions, with only the fastest denudation rates (> 30 m.Ma-1) potentially biased by the Holocene climate warming. Individual measurement uncertainties are ca. 1–2 m.Ma^{-1}. Sand sample duplicates were collected at the same location for three rivers. Differences in denudation rates between the pairs of measurements for the Layon and the Leff rivers are within their respective uncertainties. The two measurements of the Argenton site are 4.6 +/- 0.4 and 9.1 +/- 0.9 mm.ka^{-1}. This 4.5 m.Ma^{-1} difference can not be explained by individual measurement uncertainties, even at the 99% confidence level. Among the possible explanations, contamination by anthropogenic activity and sediment of artificial low concentrations cannot be excluded. In any case, the Argenton results remain within the general low erosion rate pattern. Differences in the sand / sand comparisons have no clear explanation and may simply reflect the internal variability of the erosion and sediment transport system.

The comparison of denudation rates computed for the different granulometries (Sand - Cobbles) for the same sampling site ~~,The sand / coarser sample comparison for~~ the Erdre, Douffine, and Evel yields larger differences of −3.1, 21.1 and −8.6 ~~of 3–20~~ m.Ma^{-1}, the largest differences being associated with a sand denudation rate with a large uncertainty (Douffine, σ = 5 m.Ma -1). ~~Differences in the sand / sand comparisons have no clear explanation and may simply reflect the internal variability of the erosion and sediment transport system~~. This grain-size effect has been studied systematically ~~is studied~~ in other places (e.g. Carretier et al., 2009; van Dongen et al., 2019) and is not the primary focus of our study. Given the relatively small erosion rate difference and mostly because of the small size of the dataset (n=3) and no systematism in our results we do not explore these questions further in the frame of this article. This justifies using large-scale databases to filter out such variability when deriving erosion laws (cf., Section 4.1). Hereafter, the denudation rate used for sites with sand / sand or sand / coarser samples is the average of both measurements.

The three outcropping bedrock sites show an average erosion rate of 43.6 ± 1.8 m.Ma $^{-1}$, roughly a third of the average denudation rate measured in the watersheds. This low value agrees with the ~~expected erosion behavior~~ reported lower erosion

15

rates for ridges and residuals reliefs compared to the erosion rate of the watershed where they are located (e.g., Bierman and Portenga, 2011; Dirks et al., 2016) and provides a lower bound for the local long-term erosion rate.

4. Regional models of denudation and sedimentation rates

In order to assess the amplitudes and spatial variations of uplift rates due isostatic response to surface unloading and loading processes, we construct a set of regional models of erosion and sedimentation rates that cover the whole Armorican Massif and neighboring areas up to a few hundred kilometers.

4.1. Denudation rate models

Denudation rates at the watershed scale (over 100 km^2) are controlled by a combination of the drainage basin morphology (e.g., slope, curvature), its lithology (e.g., soil cover, bedrock nature), its hydrology and dynamics (e.g., runoff, drainage migration), and its local climate (e.g., temperature, precipitation). Several global studies have attempted to define relationships between measured denudation rates and various combinations of statistically predictive parameters (Harrison, 2000; Summerfield and Hulton, 1994; Von Blanckenburg, 2005; Portenga and Bierman, 2011; Harel et al., 2016; Codilean et al., 2018). While their application domains and their results vary, these studies point out that any single parameter or multi-parameter combinations do not predict denudation rates better than within a factor of roughly two or three. Many All studies also agree suggest that the mean basin slope (or an equivalent proxy), which is very easy to compute from a DEM, is often is the often considered as the most most powerful explanatory parameter even if other geometrical parameters as the ridge curvatures, more sensitive to the DEM resolution to can also be used successfully (Hurst et al., 2012). However, the linear relationship between denudation rates and mean slopes breaks down for slope values above 25 – 30°, due to the non-linearity of sediment flux-slope relationship when slopes get closer to stability threshold (Binnie et al., 2007; Montgomery and Brandon, 2002).

In order to build our regional denudation rate models, we analyze denudation rate data for drainage basins from the Octopus database (Codilean et al., 2018) over the non-tectonic areas of Western Europe (Fig. 4a). This database is further filtered to exclude data considered not representative of our study's spatial and temporal scales: We exclude denudation rates higher than 1500 $m.Ma^{-1}$ (integration times smaller than a few hundred years), those associated with watershed areas larger than 30,000 km^2 (integration surface too large for regional modeling), and those associated with areas smaller than 100 km^2 (integration surface too sensitive to local transient processes). Our new data from the Armorican Massif complete the Octopus data-set by providing information for this up-to-now unsampled low-slope region (Fig. 4 and 5.). The final dataset comprises 220 denudation rates and morphology parameters, whose correlation is indicated in Table 2. The mean basin slopes and mean basin elevations show the highest correlations with denudation rates, in agreement with global studies. For the Armorican Massif data alone, the correlations are significantly lower, especially for the mean elevation, due to the low spread of denudation rates and morphology parameters.

Table 2. Pearson coefficient of correlations between denudation rate and basin morphological parameters

	Area	Elevation		Slope		Hypsometric Integral	Area % with slope < 1°
		mean	Standard deviation	mean	Standard deviation		
Armorican Massif	-0.27	0.25	0.42	0.51	0.48	-0.06	-0.27
Filtered Octopus + Armorican Massif	-0.23	0.82	0.72	0.76	0.75	0.40	-0.40

~~*Table 2: Denudation rate correlations with basin morphology parameters : Correlation as Pearson coefficient of correlation. For elevation and slope, correlations are given for the mean and the standard deviation (σ) of the distribution. HI: hypsometric integral. Area < 1°: percentage of basin area with slope lower than 1°. Armorican massif: new data for the Armorican Massif alone. Octopus + AM: final dataset including filtered Octopus and Armorican massif data (cf. text).*~~

Our regionally-~~filled~~continuous erosion models are built using the mean slope parameter on a ~~grid of hexagon with an area of~~rectangular 10x10 km grid -100 km^2 (roughly the minimal area of our Octopus + Armorican Massif database)~~, i.e. a grid node spacing of ca. 6 km.~~. We do not attempt to fit a process-based relationship for the prediction of erosion; rather, we derive an empirical relationship to produce a continuous erosion map from our isolated observations. The relationship between mean slope (s in °) and denudation rate (d in m·Ma^{-1}) is based on an exponential function in order to account for the nonlinearity for slope-denudation relation (Fig. 5). The best-fit function (d = 12.3 exp(0.142 s)) is associated with a root-mean-square (RMS) misfit of 22 m·Ma^{-1}, strongly controlled by the high denudation rate values (Fig. 5). For the Armorican Massif dataset alone (s < 5°), it yields a much smaller RMS misfit of 2 m·Ma-1. This function yields slightly too high results in the very-low slope area. Indeed, the predicted erosion rate for a null slope is 12.3 m.Ma-1.

We add a corrective term (-7.7 m.Ma-1) to constrain the intercept to the average value obtained from the outcrops (considered as a good proxy for minimal denudation rate). -In order to account for the variability of denudation rates for a given slope value, we also estimate two upper- and lower-bound functions that comprise 90% of the data (dmax = **4~~3~~1 exp(0.1~~3~~53~~0~~ s) and dmin = 3~~.~~5 exp(0.140 s)**). These two functions are adjusted manually to each exclude 5% of the data over the whole range of denudation rates (Fig. 5). These two boundary functions are corrected for the intercept by using the lower (-2.4) and higher (-6.5) denudation obtained from the outcrops. Adding this corrective term leads to a decrease in the RMSE of the Britanny data (from 7.24 to 6.64 m.Ma-1), and an all data-set RMSE increase from 331.2 to 332.6 m.Ma-1.

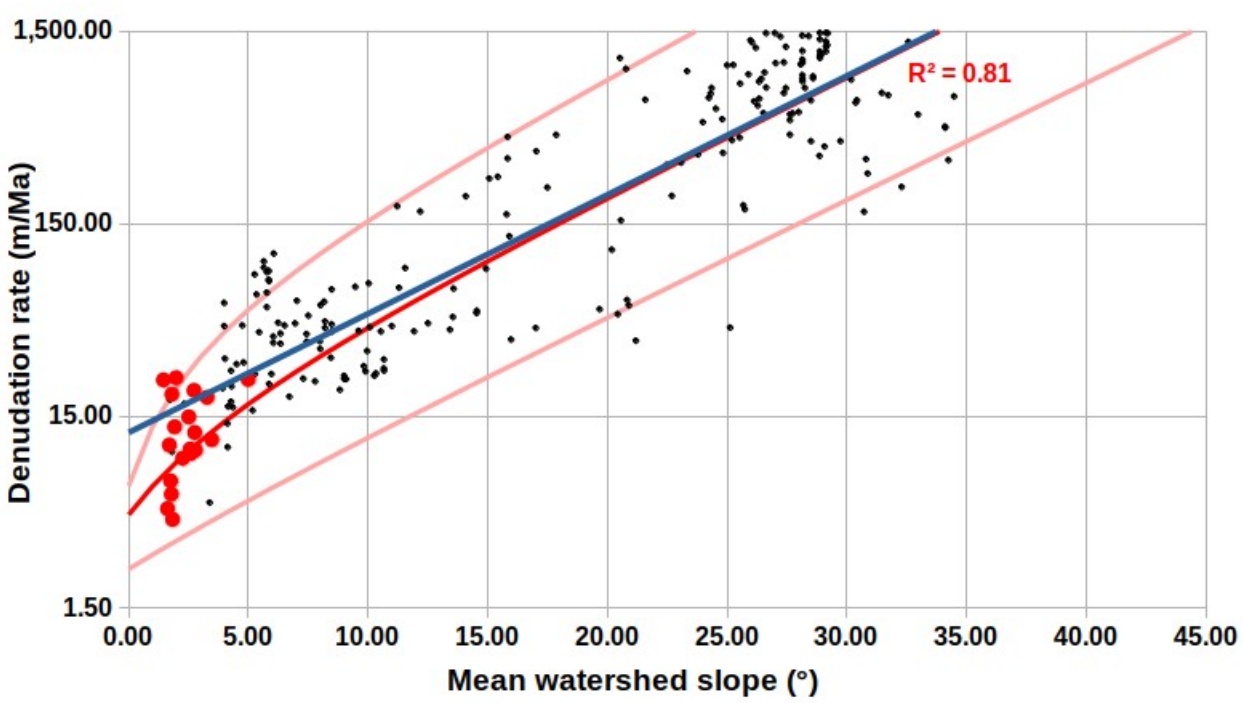

305 **Figure 5: Model of denudation rates (m Ma^{-1}) vs. mean basin slopes (°). Red and black dots are the data for the Britanny area (this study) and from the Octopus database respectively. The best-fit exponential function is in blue, the final, upper and lower boundaries are in red. The uncertainties of individual values are not represented for visualisation but typical errors for TCN are of the order of 10 %.**

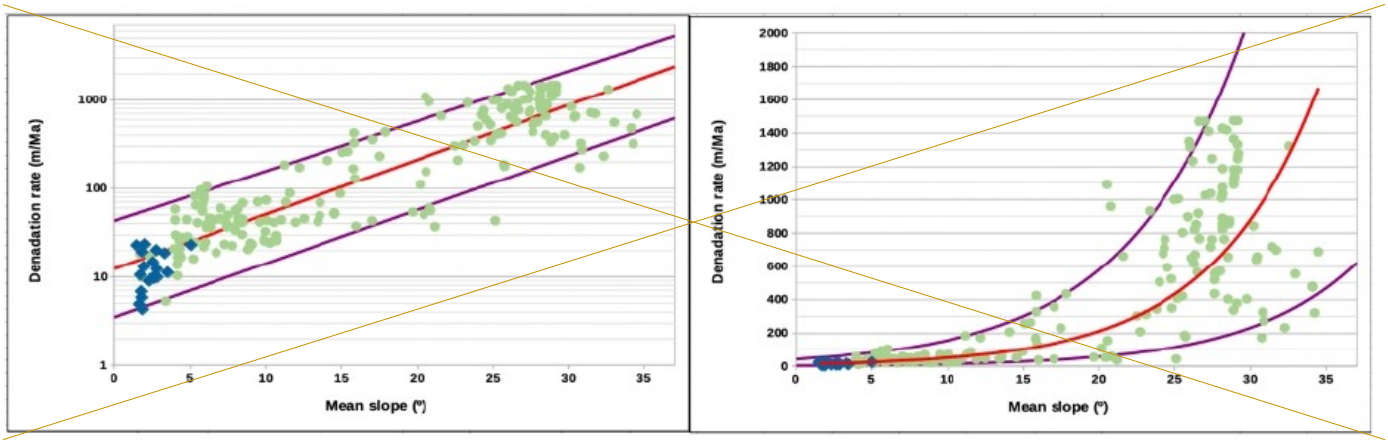

310 *Figure 5. Model of denudation rates (m Ma-1) vs. mean basin slopes (°). The left and right panels are semi-log and linear representations. Green and blue symbols are from the Octopus database and this study. Best-fit and minimum/maximum*

~~*exponential predicting functions are shown in red and purple lines (cf. Text). Typical errors for TCN measurements are of the order of 10 %.*~~

The studied area is partly associated with non quartz-bearing rocks, especially in the eastern part of the region (the Paris Basin, Fig. 2). This area is mainly composed of carbonates where the main erosional process is dissolution (Roy et al., 1999). This process being mostly located in the upper few meters, the epikarst, the slope-based relationship cannot be applied confidently. We use mean regional values to fill the synthetic model. Best estimation and associated upper and lower values are set at 18, 25 and 10 m~~/~~ Ma^{-1} respectively (Roy et al., 1999, Laignel et al., 2006). We point out that this leads to artificially homogeneous erosion rate over the carbonaceous region which is not representative of the true spatialization of the erosion but is mostly used as a proxy to circumvent possible boundary effects (see section 5.1).

We use these functions to define two denudation rate models (Fig. 6):

A mean model based on the best-fit function for all grid cells. Its denudation rates are strongly correlated with the topography and altitude on a regional scale (ca. 100 km), with relatively high rates c**a. 15–25 m·**Ma-1 in the high-altitude zones of western Brittany and northeastern Brittany-southern Cotentin, and the lowest rates ca. **5–15 m·Ma-1** in the low-altitude central region.

A random model in which each grid cell is associated with a denudation rate based randomly on the lower- bound, best-fit, or upper-bound function. This alternative model will be used to test the sensibility and potential biases of the predicted uplift rates (cf. Section 5). This model results in an average denudation rate slightly larger than that of the mean model by a factor of 1.6~~1~~1. For the non-carbonates area, this ratio is of the order of 1.6 ~~,~~due to the asymmetry of the upper- and lower-bound functions relative to the best-fit one ~~(i.e., the average of the dmin and dmax functions is 1.5 times larger than the best-fit function for the whole slope range)~~. In order to have the same total perturbation we normalized the random model by this factor 1.1 (leading to the same mean erosion rate). The random model is not correlated with topography and comprises areas of concentrations of high (c.a. 50~~–70~~ m.Ma -1) and low (c.a. 5 3~~–7~~ m.Ma-1) denudation rates over distances of 30 – 50 km interspersed between a smaller wavelength random distribution (ca. 10 km, about the grid node spacing).

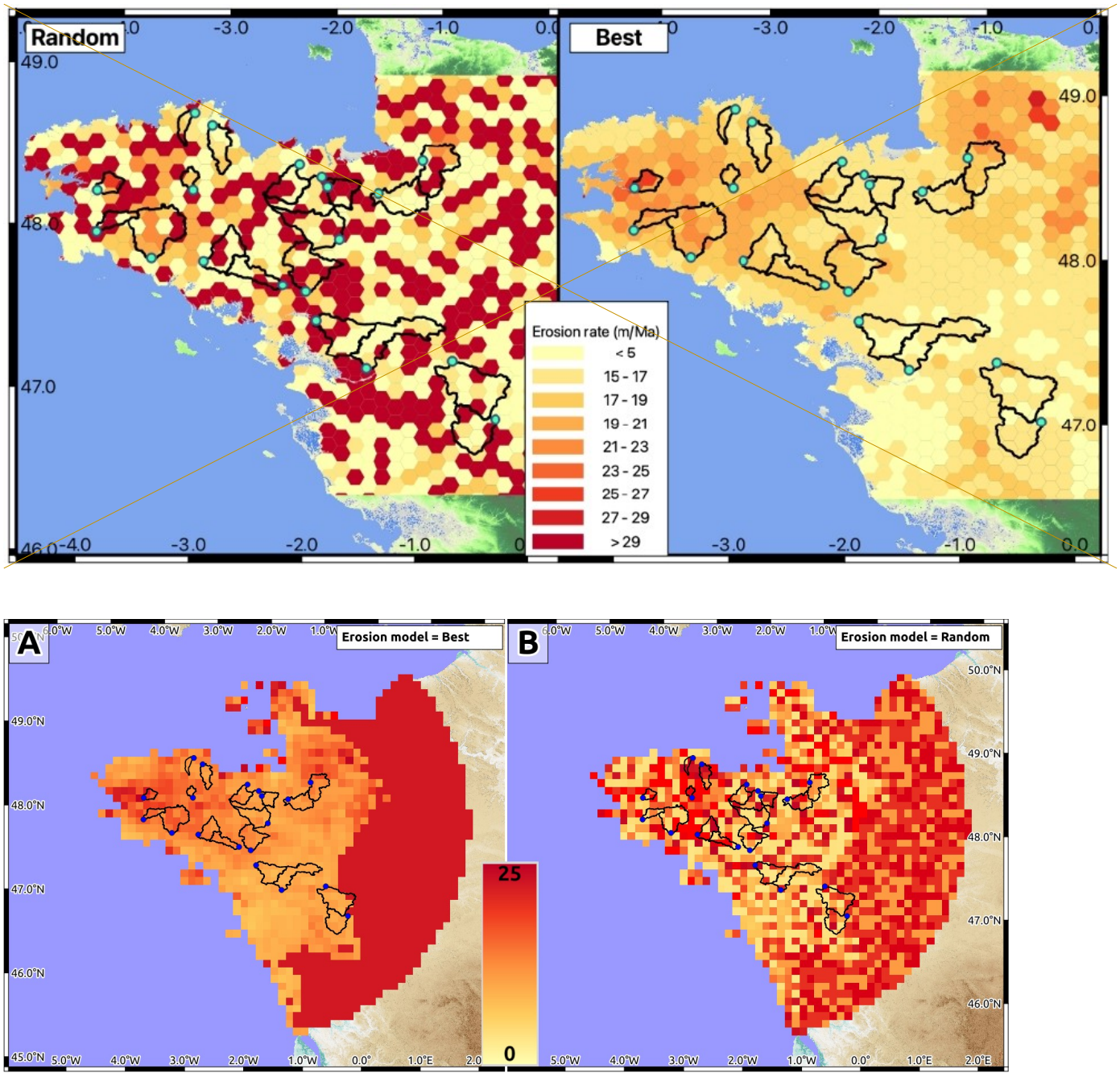

Figure 6. Best-fit and random denudation rate models. Denudation rates modeled on 100 km2 hexagons (6-km grid spacing) using the best-fit (right) and random (left) predictions models (cf. text). Sampled drainage basins and sampling locations are shown by the black outlines and blue dots.

20

Figure 6. Best-fit and random denudation rate models. Denudation rates modeled on 10x10 km rectangular grid using the best-fit (A) and random (B) predictions models (cf. text). Sampled drainage basins and sampling locations are shown by the black outlines and blue dots.

4.2. Sedimentation rates

The Pleistocene – Holocene offshore sedimentation around the Armorican Massif is characterized by two main phases: (1) near-field sedimentation along the present-day coastline during the sea-level highstands (interglacial periods) and (2) far-field sedimentation on the continental slope and rise during the sea-level lowstands (glacial periods).

The first phase corresponds to limited terrigenous sedimentation on the continental shelf, primarily at the outlet of the local rivers. Sediment types and thicknesses have been mapped using a marine geophysical and coring surveys (Augris et al., 2013a, b, c), indicating a Quaternary cover of a few meters, up to a few tens of meters in some very localized pockets at the main river mouths (Fig. 4). The English Channel (Manche) is a clear exception to this general pattern, with Quaternary sediment thicknesses up to ca. 50 m localized in the channel of the paleo Manche river. These deposits are not dated but are assumed to be the accumulation of Quaternary highstand sedimentation owing to their geological and geophysical signature (L. Simplet, pers. comm.). These 1–5 m sediment thicknesses correspond to an average sedimentation rate of ca. 0.5–2.5 $m \cdot Ma^{-1}$ over the last 2.5 Ma, with peaks up to 10–20 $m \cdot Ma^{-1}$ in the localized high-sedimentation zones. These sedimentation rates are either too low (one order of magnitude smaller than land denudation rates) or too localized to produce significant effects on land (subsidence rates of 0–2 $m \cdot Ma^{-1}$, Fig. 7).

The second phase of sedimentation corresponds to large deposits on the continental slope and rise and the oceanic basin during the Pleistocene lowstands. These large turbidite deposits correspond to the combined discharge of the main northwestern Europe rivers through the “River Manche” during the glaciation periods (Toucanne et al., 2009, 2010). The average sedimentation rates may reach a few tens of m·Ma-1 at distances of 150–250 km from the Armorican Peninsula.

5. Uplift rates driven by surface mass mobilization

5.1. Methods

The mechanical response of the lithosphere to surface mass redistribution (erosion or sedimentation) can be modeled with different assumptions, depending primarily on the time scale. For short pulses, the response can be assumed to follow that of a semi-infinite elastic body (e.g., Steer et al., 2014). At the other end of the spectrum, standard Airy or Pratt isostatic response can be considered over very long time scales of tens of million years (Haxby and Turcotte, 1976). For time scales of thousands of years to million years, the response to erosion and sedimentation is commonly modeled using a thin elastic plate overlying a low-

viscosity fluid (Champagnac et al., 2007; Stephenson and Lambeck, 1985) or using more complex elasto-visco-plastic rheologies (Vernant et al., 2013; Mazzotti et al., 2023). For domains with standard or low continental geotherm or strong rheology, the response of an elasto-visco-plastic lithosphere is close to that of an elastic plate, whereas it may differ significantly in domains with high geotherm or weak rheology (Mazzotti et al., 2023). Here we model the vertical deformation due to Late Pleistocene – Holocene erosion and sedimentation rates following the common assumption of a thin elastic plate, representing the flexural rigidity of the lithosphere. We use two approaches under this assumption, the first following a 2D formalism to study the effect of onshore erosion rates, the second based on a simpler 1D approach to test the impact of offshore sedimentation rates.

The response to erosion rates is computed using gFlex (Wickert, 2016) using the SAS scheme and NoOutsideLoads boundary conditions to produce maps of vertical velocities for our two denudation rate models coupled with a range of elastic plate thicknesses derived from rheology and from gravity-topography coherence analyses over Western Europe (Tesauro et al., 2009; Kaban et al., 2018). For the Armorican Massif and neighboring regions, these studies indicate elastic plate thicknesses varying between ca. 15–20 km and ca. 35–40 km. Lateral variations are poorly constrained and show either an eastward increase (Kaban et al., 2018) or small decrease (Tesauro et al., 2009). Thus, we test three cases of uniform elastic thicknesses of 15, 25, and 35 km to cover the observed range. Additional model parameters include the plate elastic rigidity (10 GPa) and Poisson ratio (0.25), and the crust and mantle densities (2700 and 3200 kg.m3, respectively). To determine the spatial extent of the area where we need to consider erosion or sedimentation we run several models with no erosion in the study area and 25m of erosion in the far field (Fig. 6a). We use a uniform elastic thickness of 35 km in order to have the case where the deformation will have the broadest wavelength. An erosion of 25m induces a maximum uplift of ~21m, so we choose the model where less than 1m of vertical displacement is induced in our study area (Fig. 6b). We limit the spatial extent for the emerged lands to France and do not take into account the very southern tip of the United Kingdom. For all the lands we use the mean denudation model to compute the spatial denudation rates that will be used in our model (Fig 7aNouvelle figure avec la carte des taux d'érosion ?). ~~The spatial extent of our denudation rate models (Fig. 6) is limited to the north by the Cotentin Peninsula (not included) and to the east and south by the presence of the Paris and Aquitaine sedimentary basins (not included). Based on the response pattern of a 25-km-thick elastic plate, we consider that the predicted uplift rates are valid up to ca. 50 km of the model eastern border and are thus limited to the Armorican Peninsula and the central Brittany lowland (Fig. 8).~~ The used code gFlex does not allow for direct erosion rate input, it only considers the finite response of the equivalent elastic plate to a surface perturbation. In order to estimate an uplift rate we use the following rationale: the finite flexural response to a given load is equal to the sum of numerous smaller loads applied on the same plate. In other words, the gFlex solution for a 100 m unloading (for example representative of the total erosion over 1 Ma) is equal to the sum of 100 times the flexure associated with a 1 m unloading (equivalent to 10 cm/ka). If the mantle viscosity is to be accounted for, the two solutions will diverge as the flexure associated with the last erosional step will not be totally achieved due to the mantle viscosity. This effect however is considered negligible for Ma-time scale as characteristic mantle relaxation time is of the order of 10^5 yrs leading to less than 1% error for an 1 Ma equivalent modeling. The sedimentation impact is tested using the 1D solution for an infinite elastic plate subjected to a punctual load (Turcotte and Schubert, 2014). This 1D model uses a Te value of 25 km and is associated with three sedimentation profiles, each

representative of given sedimentation patterns and periods: (1) A coastal sedimentation rate of 20 m Ma^{-1} extending 10 km offshore from the coast, as an estimation of the maximum current sedimentation.(2) A continental shelf sedimentation rate of 2 m Ma^{-1}, from the coast to 40 km offshore, representative of the mean Quaternary highstand sedimentation. (3) A continental slope sedimentation rate of 30 m Ma-1 localized 170 to 270 km offshore, representatives of the Quaternary lowstand sedimentation. These sedimentation models are compared with an onshore erosion rate of 15 m Ma-1 extending 125 km from the coast.

A primary assumption of both 1D and 2D models is that erosion and sedimentation rates are considered to be constant through time, thus generating an elastic (time independent) response of the lithosphere. This simplification does not allow taking into account temporal variations of erosion or sedimentation on time scales of 10^{3} – 10^{4} years, such as those associated with climate changes during glacial / interglacial transitions. These transient effects would generate a response similar to that of classical postglacial rebound processes, mainly depending on the upper mantle effective viscosity structure (e.g., Peltier, 2022). However, both data and modeling framework are lacking at this stage to integrate these types of variations in our study.

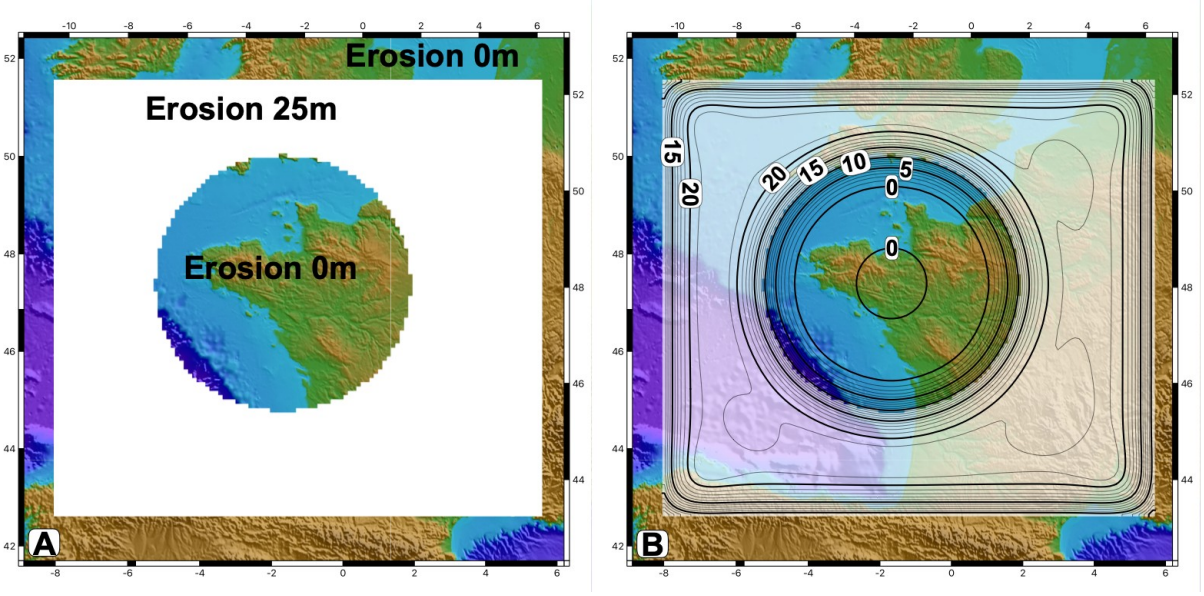

Figure 7 : example of numerical modeling sensitivity test. Panel A is the input denudation rates. Panel B is the bending solution from the code with iso-bending contour (m).

5.2 Effect of offshore sedimentation

Based on the 1~~2~~D model, we estimate that the effect of offshore sedimentation patterns on vertical velocities on land is ca. 0.5–1 m·Ma-1 (subsidence rate for near-shore sedimentation or uplift rate for slope sedimentation), about ten times smaller than the effect of denudation rates (Fig. 8~~7~~). Due to the very low effects of the sedimentation rates on land vertical motions and to the sparse distribution of sediment thickness mapping, we do not include the sedimentation rates in the following models. Depending on the interaction of the sedimentation patterns, this could lead to a small overestimation of ca. 5–15 % of the uplift

rates along the coast and less than 5% further inland (Fig. 8~~7~~). This effect should be kept in mind when discussing specific model predictions along the coast.

Figure 8 : Schematic 2D models of uplift rates due to on-land erosion rates and offshore sedimentation rates. Uplift rates (Vz) shown as a function of distance (x) along a schematic 2D South-North profile across the Armorican Peninsula, with the gray area indicating the land section. The black curve shows uplift rates due on-land erosion rate of 15 m.Ma -1 (0 ≤ x ≤ 125 km). The green, orange, and blue curves show uplift rates due to three sedimentation rate scenarios: 2 m.Ma-1 on a 40 km-wide coastal section (-40 ≤ x ≤ 0 km), 20 m.Ma-1 on a 10 km-wide coastal section (-10 ≤ x ≤ 0 km), 30 m.Ma-1 on a 100 km-wide continental slope section (-270 ≤ x ≤ -170 km). Uplift rates are given for an elastic plate thickness of 25 km (cf. Section 5). Dashed lines above the graph show locations of the erosion / sedimentation zones.

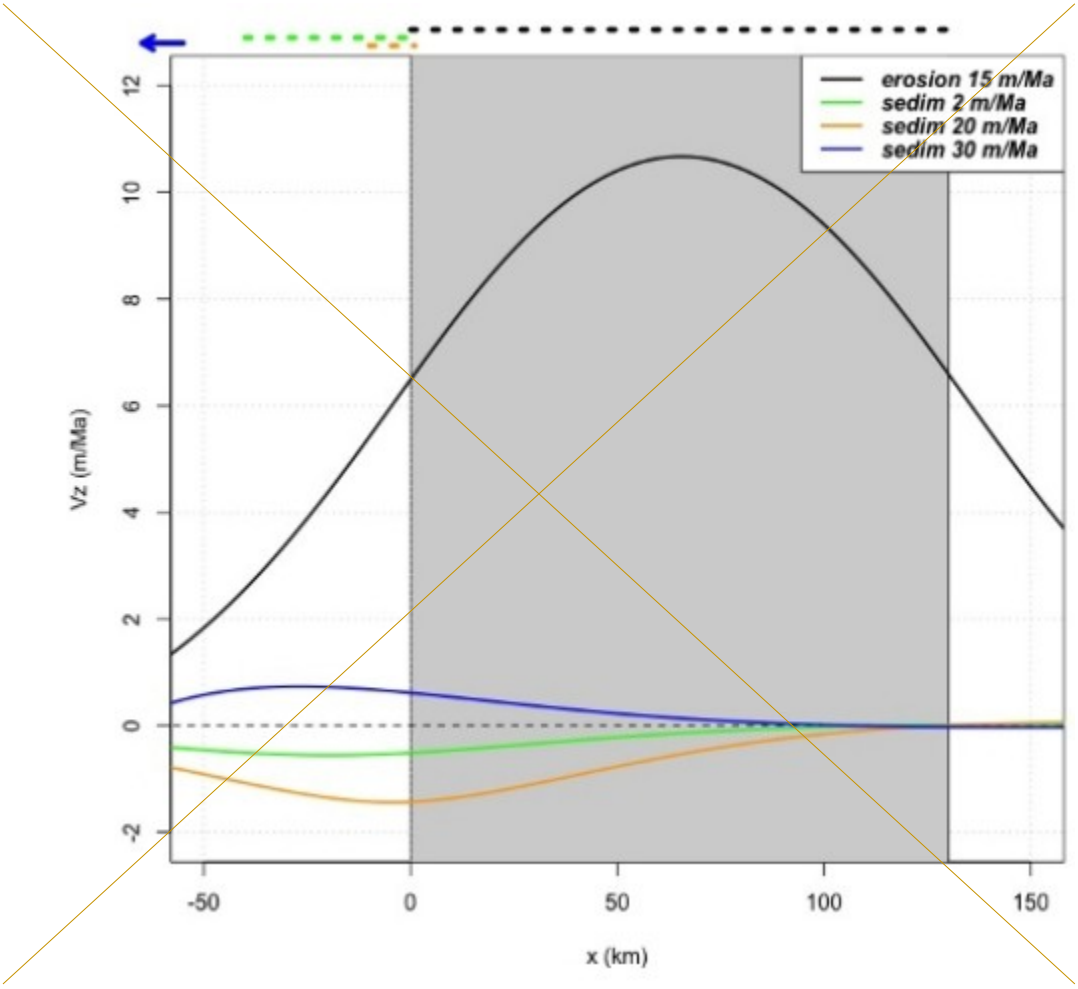

Figure 7. Schematic 2D models of uplift rates due to on-land erosion rates and offshore sedimentation rates. Uplift rates (Vz) shown as a function of distance (x) along a schematic 2D South-North profile across the Armorican Peninsula, with the gray area indicating the land section. The black curve shows uplift rates due on-land erosion rate of 15 m.Ma -1 (0 ≤ x ≤ 125 km). The green, orange, and blue curves show uplift rates due to three sedimentation rate scenarios: 2 m.Ma-1 on a 40 km-wide coastal section (-40 ≤ x ≤ 0 km), 20 m.Ma-1 on a 10 km-wide coastal section (-10 ≤ x ≤ 0 km), 30 m.Ma-1 on a 100 km-wide continental slope section (-270 ≤ x ≤ -170 km). Uplift rates are given for an elastic plate thickness of 25 km (cf. Section 5). Dashed lines above the graph show locations of the erosion / sedimentation zones.

5.3. Effect of onshore erosion

Figure 98 (A, B, C) shows the uplift rates predicted for the mean denudation rate model associated with the three elastic thickness cases. All three models show maximum uplift rates ca. 8~~12~~–15 m.Ma^{-1} centered on the western~~central~~ Brittany highland~~lowland~~. The uplift rates decrease sharply westward down to ~ 5~~–4–10~~ m.Ma $^{-1}$ near the coast ~~in the Armorican Peninsula~~, with a decrease gradient controlled by the elastic plate thickness (lower gradient for thicker plate). The Central lowland region is associated with an uplift rate of 6 – 8 m.Ma^{-1}. This value is weakly dependent on the Te value. The East-West gradient however is strongly dependent to the Te value because for small Te (15 km, Fig. 8A), the uplift rate is almost twice highet in the western highland while for Te of 35 km (Fig. 8C), almost no East-West gradient can be observed. ~~The eastward evolution is strongly dependent on the Te value because the Central Lowland can either be associated with a low uplift area (low Te value, Fig.8 A) or in the middle of a nearly constant uplift area (Fig. 8 C).~~ This latter pattern is simply explained by the fact that uplift rates in central Brittany are due to the combined effects of erosion rates in all directions, whereas uplift rates in the Armorican Peninsula are only due to erosion rates in the peninsula itself, thus producing a smaller combined effect. Uplift rates along the Armorican Peninsula coastline are ca. 6~~8~~ m.Ma -1 in the northeast (Saint-Malo, Saint-Brieuc) and southeast (Lorien, Saint-Nazaire) regions. They diminish to 5~~4–6~~ m.Ma-1 along the western tip of the peninsula (Roscoff, Brest, Concarneau). The smallest plate-thickness model (Te = 15 km) shows a characteristic elongated pattern of uplift rate ca. 10–13 m.Ma^{-1} along the peninsula east-west axis. This pattern progressively disappears in the thicker plate models (Te = 25 km and Te = 35 km) due to the low-pass filtering effect of the elastic plate response that smooths out the erosion rate spatial distribution.

The random model allows us to test two effects: (1) the ~~sensibility~~sensitivity of the predicted uplift rates to the spatial distribution of denudation rates, and (2) the possible bias of uplift rates due to the nonlinear slope-denudation rate relationship. Figure 8D shows an example of uplift rates associated with a random denudation rate distribution (Fig.6A) for a plate thickness Te = 25 km. The uplift rate pattern is similar in shape to that of the mean model, albeit with rates ca. 1.5–1.7 times larger depending on the locations along the peninsula due to the denudation rates being on average 1.6 times larger than those of the mean model (cf. Section 4). This model illustrates two important points:

Spatial variations in denudation rates at dimensions of 10–50 km are filtered out by the flexural rigidity of the lithosphere and are not reflected in the uplift rates. This corresponds to a minimum sensitivity length that varies with the elastic plate thickness but in our case (Te = 15–35 km) remains ca. 50 km.

25

Considering the uncertainties in denudation rates and the 90% envelope derived from our analysis of stable Western Europe data (Section 4), the random model results provide an upper bound for predicted uplift rates at any given point on the map (but not on average).

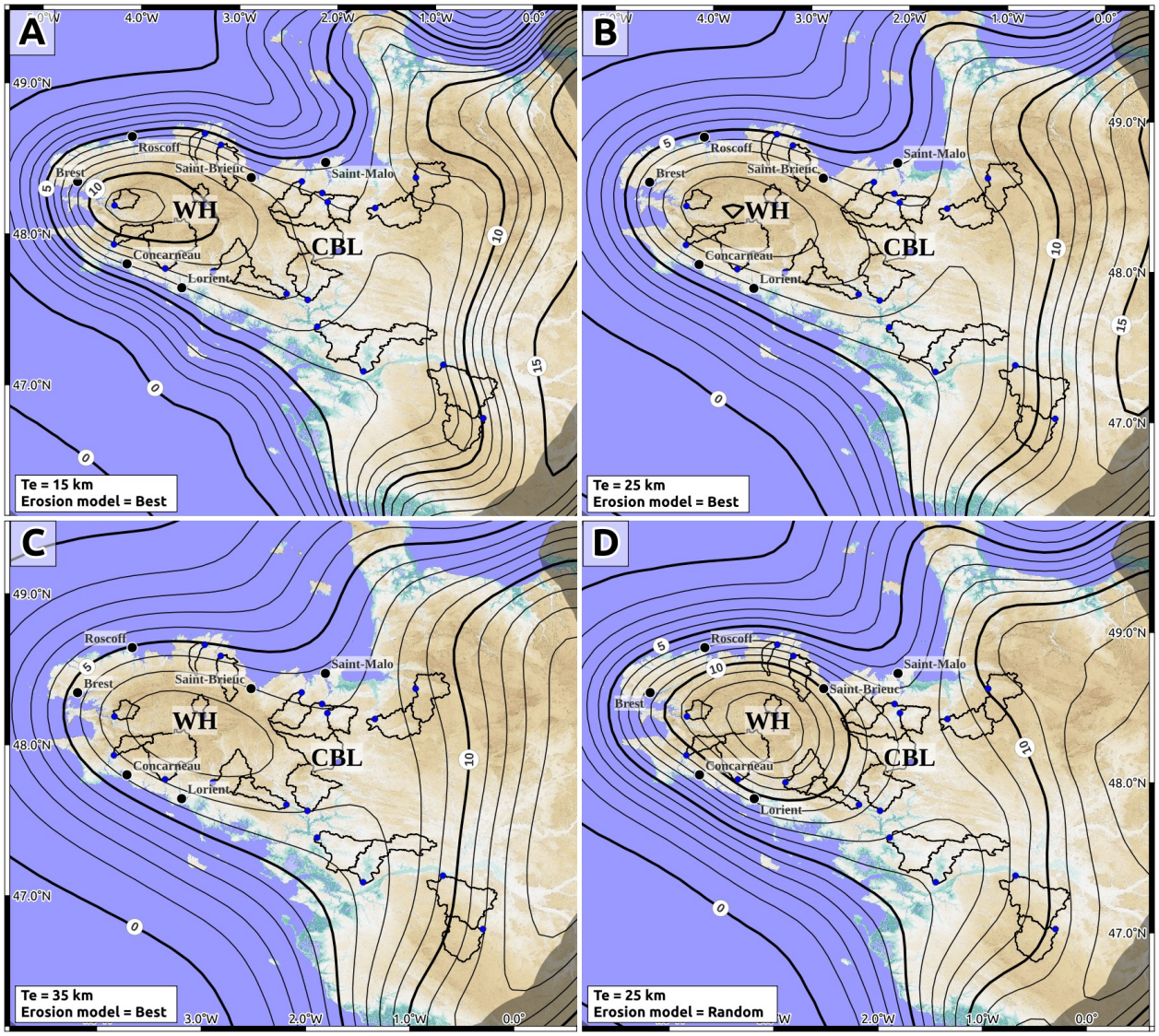

Figure 9. Predicted Late Pleistocene – Holocene uplift rates due to denudation rates. Isocontours of uplift rates in m.Ma-1. A, B, C: Best-fit erosion model and three elastic plate thicknesses (15, 25, 35 km). D: Random erosion model and 25 km elastic plate thickness. The grey area on the east side shows where uplift rates are biased by model border effects and must not to be considered. CBL and WH stands for Central Britanny Lowland and Western Highland respectively.

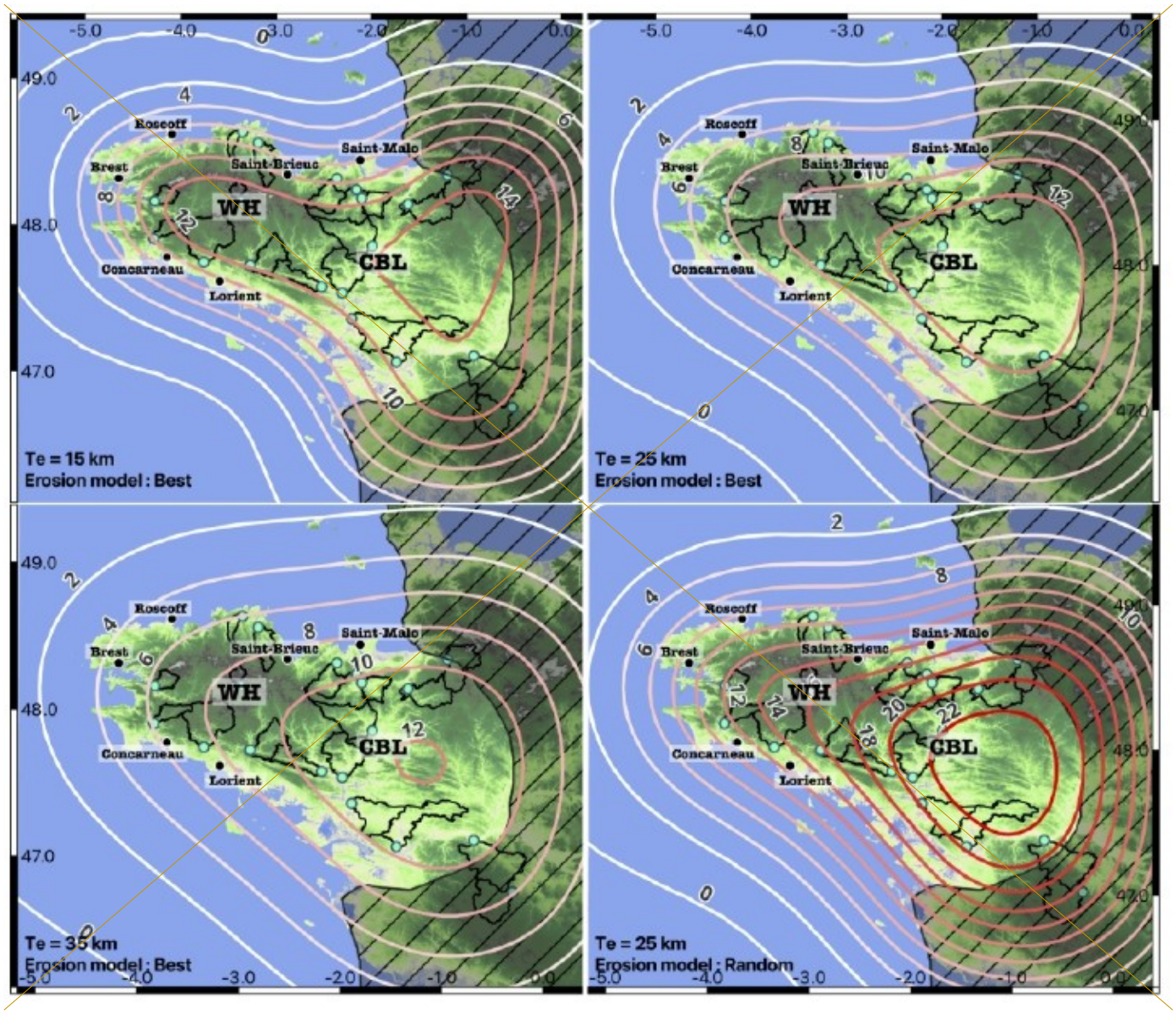

Figure 8. Predicted Late Pleistocene – Holocene uplift rates due to denudation rates. Isocontours of uplift rates in m.Ma-1. A, B, C: Best-fit erosion model and three elastic plate thicknesses (15, 25, 35 km). D: Random erosion model and 25 km elastic plate thickness. The grey dashed area on the east side shows where uplift rates are biased by model border effects and must not to be considered. CBL and WH stands for Central Britanny Lowland and Western Highland respectively.

6. Discussion

6.1. Regional denudation and erosion rate variability

Despite the uncertainties on individual denudation rate estimations, we can rely on local and regional averages to identify significant spatial variations. The main signal in the Armorican Massif is the difference between the western highland and central lowland regions. The eight drainage basins fully or primarily eroding the western highland region (Blavet, Claie, Douffine, Evel, Laita, Leff, Odet, and Guindy) show an average denudation rate of 13 ± 6 m.Ma^{-1}. In contrast, the nine basins eroding the central lowland (Aff, Argenton, Couesnon, Erdre, Isac, Layon, Linon, Meu, Selune) show an~~d~~ average rate of 7 ± 4 m.Ma^{-1}. No other geographical pattern, such as a north-south difference, can be identified. Although its statistical power is low, the difference of factor of 2 in denudation rates between the western highlands and the central lowlands can easily be explained by the small difference in elevation and in relief between the two areas. This result is in good agreement with Bonnet et al. (1998) and Lague et al. (2000) who proposed higher incision and erosion rates by a factor of about 1.5–2 in the western highland compared to the central lowland based on quantitative morphological analyses of the topography.

This spatial variability is also consistent with the estimations of the mean annual sediment export of rivers in these two areas (Delmas et al., 2012). The average export of rivers primarily associated with the western highland is ca. 0.17 Mt.yr^{-1}, about twice as large as that of the Vilaine River located in the central lowland (ca. 0.07 Mt.yr $^{-1}$). Considering the respective areas of these two drainage systems, and assuming a sediment density of 1400 kg.m^{-3}, the equivalent erosion rates of the western and central regions are ca. 10 and 5 m.Ma $^{-1}$, about 60% of our average denudation rates. Such a difference is commonly observed in studies comparing cosmogenic denudation rates with sediment fluxes (e.g., Kirchner et al., 2001), due possibly to the different sampling time scales of the two methods or to the fact that denudation rates sample both chemical and mechanical erosion processes while suspended sediment flux data lack the dissolved load.

A possible source of error in the regional denudation pattern is the presence of the Falluns deposits. Indeed, as these deposits are relatively young, the absence of inheritance in terms of ^{10}Be concentration cannot be totally ruled out. If existent, this inheritance diminishes the apparent denudation rate (the true current denudation rate being higher). However, we do not believe this inheritance to be of a high impact, if any. Indeed, first, the majority of the region, notably the western part, is associated with the total absence of such deposits. Second, the Falluns deposits are principally associated with carbonates, therefore the total quartz-bearing mass is expected to be small. Third, a significant part of the finer part of it being, removed during the sampling or latter chemical purification.

6.2. Late Pleistocene – Holocene uplift rates, regional sea level, and geodynamics

Based on present-day elevations of MIS 11 and MIS 5e marine terraces, Pedoja et al. (2018) estimate mean Middle Pleistocene and Upper Pleistocene apparent uplift rates of 50 ± 10 m.Ma^{-1} for most of Western Europe coastline, from southern England to Portugal. Using morpho-stratigraphic evidence, they argue that these data cannot be explain~~ed~~ solely by eustatic sea-

level variations and require a mean uplift rate of ca. 10 m.Ma^{-1}, due to an “increasing lithospheric compression that accompanies Cenozoic orogenies”.

Around the Armorican Peninsula, elevated marine terraces of MIS 5e age are found at an average elevation of 6 ± 2 m (full range 4–14 m, data from Pedoja et al. (2018) compilation). Glacial isostatic adjustment corrections and fingerprinting effects of past icesheets render the estimation of regional Late Pleistocene sea levels particularly difficult (Hay et al., 2014). Relative to present-day sea level, MIS 5e eustatic elevations are estimated ca. 2–9 m at 123–125 ka (with preferred value of 4.5–7.5 m) and ca. -20 m at 113 ka, with a likely intermediate highstand ca. 5 m at 116–188 ka (Kopp et al., 2013; Polyak et al., 2018; Hay et al., 2014). Assuming a regional eustatic sea level of 2, 4.5, 7.5, or 9 m results in a average ~~Late Pleistocene~~ uplift rate since the Late Pleistocene of -23, -12, 12, or 31 m.Ma^{-1}, respectively, for the Armorican Peninsula marine terrace (average elevation of 6 m). In comparison, we estimate uplift rates of 4–8 m.Ma^{-1} (upper bound of 6–14 m.Ma^{-1}) due to the response to denudation rates (Fig. ~~8~~9).

Thus, within the uncertainties associated with the different sea level estimations, erosion-driven uplift can explain the uplifted Upper Pleistocene marine terraces around the Armorican Peninsula, without a need for additional geodynamic processes ~~creating~~promoting uplift. Another way to consider these results is that, if denudation alone drives the uplift of the Armorican Peninsula coastline, the elevation of the marine terraces constrains the regional Upper Pleistocene sea level to a highstand ca. 5 m. ~~A third interpretation is that additional uplift due to other geodynamic processes (in addition to erosion) would require a low regional eustatic sea level (2–5 m).~~

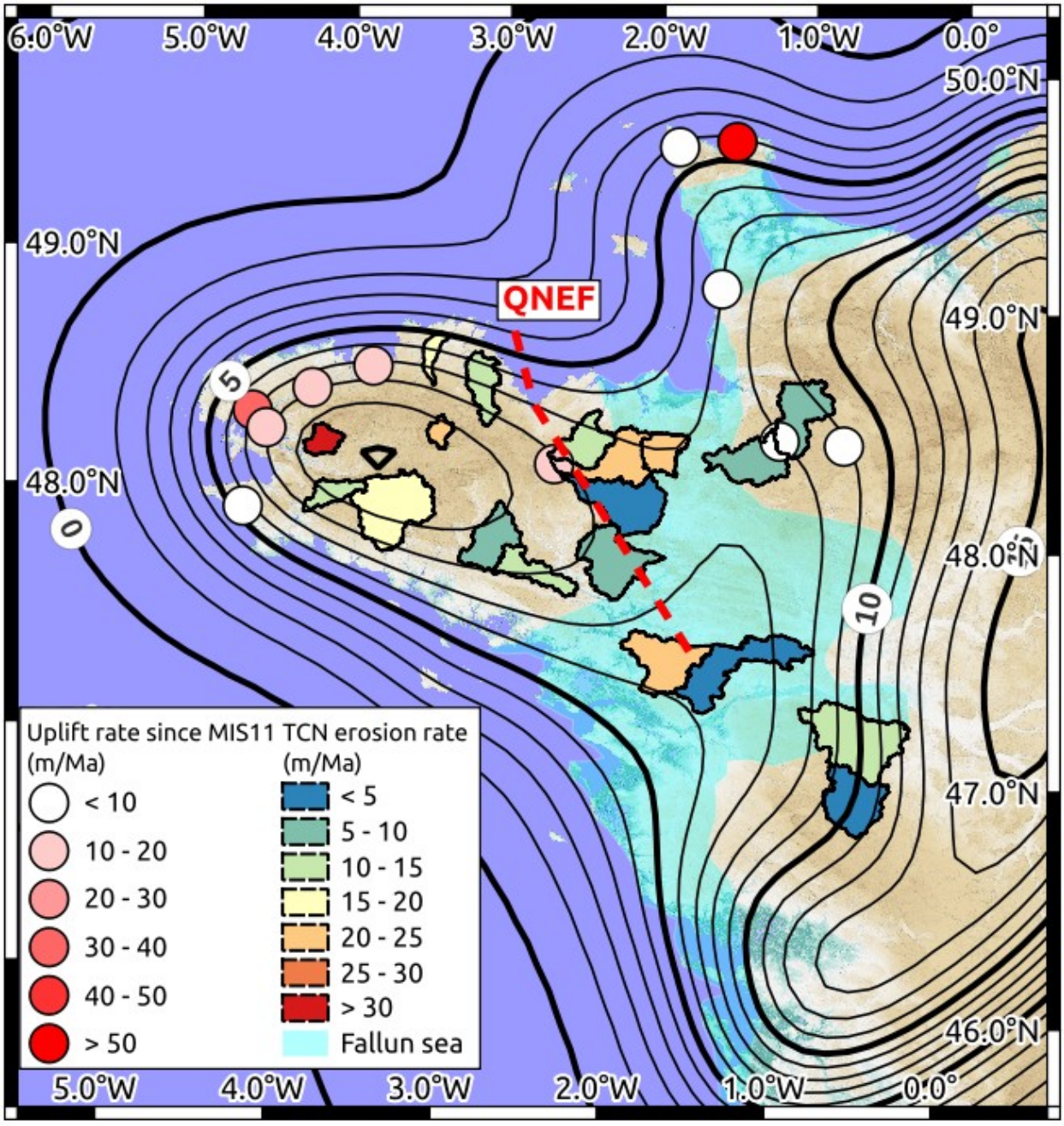

Figure 10 : Summary of the measured denudation rate, derived uplift rate due to erosional isostatic adjustment and observed uplifted marine terraces (from Pedoja et al., 2018). The flexural response to erosion is provided for a Te = 25 km and the best synthetic erosional model. QNEF is the Quesnoy-Nort-sur-Erdre Fault.

30

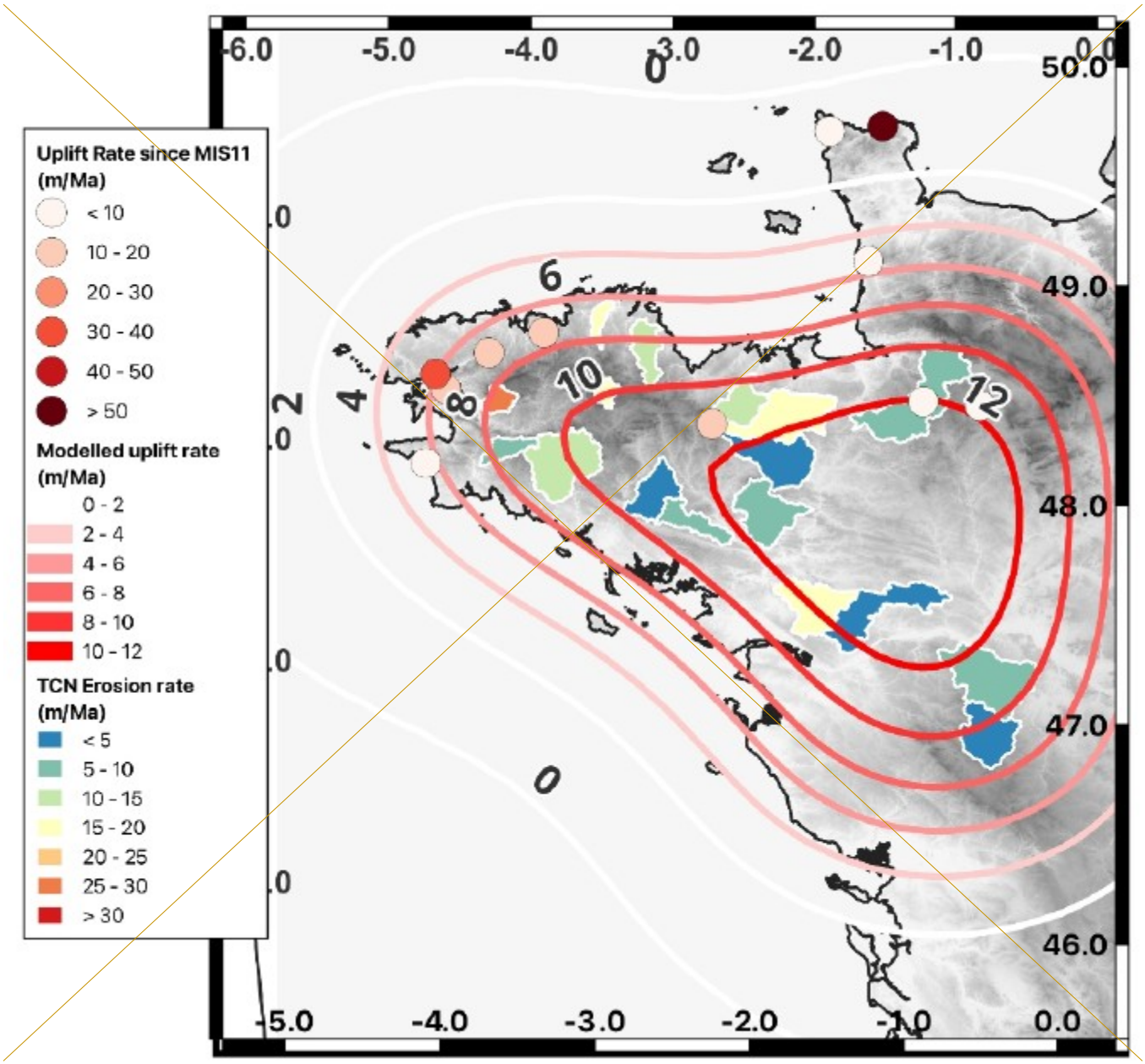

Figure 9 : Summary of the measured denudation rate, derived uplift rate due to erosional isostatic adjustment and observed uplifted marine terraces (from Pedoja et al., 2018). The flexural response to erosion is provided for a Te = 25 km and the best synthetic erosional model.

6.3. Quaternary morphology and tectonics

The elevations of marine deposits, corrected for past eustatic sea level, provide first-order estimations of Quaternary uplift rates in the central lowland region of the Armorican Massif (Section 2). They indicate an average uplift rate of 4–13 m·Ma^{-1} since ca. 3 Ma (Brault et al., 2004) or 16 ± 2 m·Ma^{-1} average during the Pleistocene (Bessin et al., 2017). If we assume that our denudation rates are representative of the Quaternary period (mix of glacial and interglacial periods), these geological uplift rates are in good agreement with those predicted in response to erosion (ca. 12–15 m.Ma^{-1}, upper bound ca. 20 m.Ma^{-1}, Fig. 8). As for the Upper Pleistocene marine terraces, this comparison suggests that erosion-driven uplift is enough to explain the elevated Quaternary marine markers.

The pattern of uplift rates due to denudation rates also points out a minor difference between the western highland (ca. 86–124 m.Ma^{-1}) and the central lowland (ca. 12–156-8 m/Ma $^{-1}$), depending on the assumed lithosphere equivalent elastic thickness (Fig. 8). Combined with the opposite pattern of denudation rates (ca. 2016 and 158 m.Ma^{-1} in the western and central regions, respectively, Fig. 6), these results suggest a quasi-stationary surface elevation in the central lowland (close to the landscape equilibrium status) whereas the absolute elevation of the western highland region diminishes by ca. 5-10 m.Ma $^{-1}$. These very low rates of topographic evolution indicate a persistence of the present-day east-west elevation differences throughout the Quaternary, despite the Mid Pleistocene reconfiguration of the drainage network (Guillocheau et al., 2003; Brault et al., 2004). As stated, the low-elevation area is associated with an uplift-rate of the same value as the denudation rate hence providing a first indication for landscape equilibrium. In the peninsula itself, the uplift rate is lower than the denudation rate supporting a probable non-equilibrium of the landscape (this feature is also supported by the morphology with significant, very localized incisions). The discrepancy between the low-elevation area and high-elevation are is not clearly elucidated and can be interpreted for instance and not exclusively one of another, as an initial differential uplift (of an unknown age), an erodibility contrast leading to achieved equilibrium in the central low-land part and not yet in the peninsula one.

The question of a potentially differential uplift rates across the QNEF system, accommodating 10 – 60 m.Ma^{-1} of east-side-down relative vertical motion, proposed by Bonnet et al. (1998) and Lague et al. (2000) is hardly in agreement with our results. If we found a possible higher uplift rate on the western side of the QNEF, the differential is likely to be no more than a few m.Ma^{-1} if erosion alone drives Quaternary uplift, as suggested by the agreement with the Cenozoic marine deposits. Additional processes such as local tectonics could induce the proposed differential uplift rates and QNEF system motion. However, this would result in differential altitudes of ca. 1.5 – 8 m of the MIS 5e marine terraces on both sides of the QNEF system along the northern Armorican Peninsula coast. The variability in the local terrace uplift rate precludes a robust conclusion, but they do not show a clear east-west difference in altitudes (Fig. 9). An alternative explanation is to consider that the east-west difference in incision rates observed by Bonnet et al. (1998) and Lague et al. (2000) is not due to a major difference in uplift rates, but to a difference in the erodibility. The eastern region has a mean higher erodibility, notably due to the initial presence of the Fallun deposits. This higher erosional efficiency may have resulted in fast erosion processes post 2 Ma, and thus present-day low erosion and incision rates associated with a smooth landscape. In contrast, the western highland was

characterized by higher relief and lower (bedrock) erodibility ca. 2 Ma, and thus may still currently be in a transient state of higher erosion and incision rates.

Overall, the lack of marine deposits in the western highland, the variability in the marine terrace data and the coarse information from our study preclude distinguishing between the two propositions and the potential activity, or not, of the QNEF system.

7. Conclusion

In the Armorican Massif, denudation rates measured from terrestrial cosmogenic nuclide concentrations range between 3 and 3327 m.Ma^{-1}. These rates are representative of the Late Pleistocene (20–200 kyr). On average, the western highland region of the Armorican Massif shows denudation rates about twice those of the central lowland region (13c.a. 15 ± 6 m.Ma^{-1} vs. c.a. 7 ± 4 m.Ma^{-1}, Fig. 910), in general agreement with previous regional morphology and erosion studies (Bonnet et al., 1998; Lague et al., 2000; Delmas et al., 2012). There is no clear denudation signal associated with large-scale tectonic structures (e.g., South-Armorican Shear Zone, Quessnoy-Nort-sur-Erdre Fault). The lithosphere flexural isostatic response to these ongoing denudation rates results in an overall uplift of the Armorican Peninsula. Predicted uplift rates range from ca. 126–815 m.Ma-1 in the central lowland region to ca. 48 – 120 m.Ma^{-1} in the western peninsula and ca. 4–8 m.Ma^{-1} along the coast (Fig. 109). Considering the uncertainties in eustatic sea-level corrections, these erosion-driven uplift rates can explain the uplifted Late Pleistocene marine terraces along the Armorican Peninsula coastline (Pedoja et al., 2018), without necessitating additional geodynamic processes such as regional compression or local active faults. While our results do not preclude the existence of such other processes, they show that, if present, their effects must be much slower than previously proposed (Bonnet et al., 1998). Finally, assuming that they can be extrapolated over the whole Pleistocene period, the erosion-driven uplift rates in the central lowland region are also sufficient to explain the elevated Quaternary marine deposits (Brault et al., 2004; Bessin et al., 2017).

Our results show that long-term erosion over the Holocene and Pleistocene can be a major driver of the observed uplift in the Armorican Peninsula and, likely, in other stable continental regions. While other geodynamics processes may also contribute to these uplift rates, spatial variations in erosion rates should be taken into account for before trying to derive global or regional geodynamic or tectonic conclusions (Gurnis et al., 2000; Pedoja et al., 2011; Murray-Wallace et al., 1996; Bonnet et al., 2000). They also suggest that the role of long-term erosion as a driver or promoter of intraplate seismicity should be considered in the Armorican Peninsula and other stable continental regions (Gallen and Thigpen, 2018; Mazzotti et al., 2023).

Author contributions.

O. M. and S. M. performed the field work and sampling. O. M. and V. G. performed the sample preparation. O. M. and S. M. performed the initial data analysis and draft of the manuscript. All authors discussed the result, the data analysis and commented on the manuscript.

Competing interests.

The contact author has declared that none of the authors has any competing interests.

Acknowledgments

This study was supported by the French “Agence Nationale de la Recherche”, project ANR-20-CE01-0005 “EroSeis”. Models, data analyses, and figures were done with open-source, free software (https://www.python.org/, https://www.qgis.org/, https://github.com/awickert/gFlex). Model parameters and results are available on demand on the Open Science Framework “EroSeis” project (https://osf.io/yq3bt/). We thank Laure Simplet (Ifremer) for providing the sedimentation databases and information, and Samuel Toucanne (Ifremer) for the Fleuve Manche references. *ASTER AMS is part of the LN2C national facility (CEREGE, Aix-en-Provence). It is supported by INSU/CNRS, IRD and AMU, and is a member of the REGEF and Plateforme Aix-Marseille networks.*

Bibliography

Arnold, M., Merchel, S., Bourlès, D. L., Braucher, R., Benedetti, L., Finkel, R. C., Aumaître, G., Gottdang, A., and Klein, M.: The French accelerator mass spectrometry facility ASTER: Improved performance and developments, Nucl. Instrum. Methods Phys. Res. Sect. B Beam Interact. Mater. At., 268, 1954–1959, https://doi.org/10.1016/j.nimb.2010.02.107, 2010.

Augris, C., Simplet, L., and Gautier, E.: Isopaques de bancs sableux en Mer du Nord, Manche et Atlantique, https://doi.org/10.12770/75AD486F-9D03-4FEB-B742-BE6C6F791345, 2013a.

Augris, C., Simplet, L., and Gautier, E.: Isopaques de couverture indifférenciée en Mer du Nord, Manche et Atlantique, https://doi.org/10.12770/C841CA37-B414-4C51-AD6A-16BC34E8CF6F, 2013b.

Augris, C., Simplet, L., and Gautier, E.: Isopaques de nappes alluviales en Mer du Nord, Manche et Atlantique, https://doi.org/10.12770/6C4CCD44-71B1-411D-91D1-ECCD1B2A46F1, 2013c.

Balco, G., Stone, J. O., Lifton, N. A., and Dunai, T. J.: A complete and easily accessible means of calculating surface exposure ages or erosion rates from 10Be and 26Al measurements, Quat. Geochronol., 3, 174–195, https://doi.org/10.1016/j.quageo.2007.12.001, 2008.

Ballèvre, M., Bosse, V., Ducassou, C., and Pitra, P.: Palaeozoic history of the Armorican Massif: Models for the tectonic evolution of the suture zones, Comptes Rendus Geosci., 341, 174–201, https://doi.org/10.1016/j.crte.2008.11.009, 2009.

Bessin, P., Guillocheau, F., Robin, C., Schroëtter, J.-M., and Bauer, H.: Planation surfaces of the Armorican Massif (western France):Denudation chronology of a Mesozoic land surface twice exhumed in response to relative crustal movements between Iberia and Eurasia, Geomorphology, 233, 75–91, https://doi.org/10.1016/j.geomorph.2014.09.026, 2014.

Bessin, P., Guillocheau, F., Robin, C., Braun, J., Bauer, H., and Schroëtter, J.-M.: Quantification of vertical movement of low elevation topography combining a new compilation of global sea-level curves and scattered marine deposits (Armorican Massif, western France), Earth Planet. Sci. Lett., 470, 25–36, https://doi.org/10.1016/j.epsl.2017.04.018, 2017.

Beucler, É., Bonnin, M., Hourcade, C., Van Vliet-Lanoë, B., Perrin, C., Provost, L., Mocquet, A., Battaglia, J., Geoffroy, L., Steer, P., Le Gall, B., Douchain, J.-M., Fligiel, D., Gernigon, P., Delouis, B., Perrot, J., Mazzotti, S., Mazet-Roux, G., Lambotte, S., Grunberg, M., Vergne, J., Clément, C., Calais, É., Deverchère, J., Longuevergne, L., Duperret, A., Roques, C., Kaci, T., and Authemayou, C.: Characteristics and possible origins of the seismicity in northwestern France, Comptes Rendus Géoscience, 353, 53–77, https://doi.org/10.5802/crgeos.86, 2021.

Binnie, S. A., Phillips, W. M., Summerfield, M. A., and Fifield, L. K.: Tectonic uplift, threshold hillslopes, and denudation rates in a developing mountain range, Geology, 35, 743, https://doi.org/10.1130/G23641A.1, 2007.

Portenga, E. W., Bierman, P. R., Understanding Earth's eroding surface with 10 Be. GSA today. Aug;21(8):4-10. https://doi.org/10.1130/G111A.1. 2011

Bonnet, S., Guillocheau, F., and Brun, J.-P.: Relative uplift measurement using river incisions: the case of the Armorican basement (France), Comptes Rendus Académie Sci. - Earth Planet. Sci., 327, 245–251, 1998.

Bonnet, S., Guillocheau, F., Brun, J.-P., and Van Den Driessche, J.: Large-scale relief development related to Quaternary tectonic uplift of a Proterozoic-Paleozoic basement: The Armorican Massif, NW France, J. Geophys. Res. Solid Earth, 105, 19273–19288, https://doi.org/10.1029/2000JB900142, 2000.

Braucher, R., Guillou, V., Bourlès, D. L., Arnold, M., Aumaître, G., Keddadouche, K., and Nottoli, E.: Preparation of ASTER in-house 10Be/9Be standard solutions, Nucl. Instrum. Methods Phys. Res. Sect. B Beam Interact. Mater. At., 361, 335–340, https://doi.org/10.1016/j.nimb.2015.06.012, 2015.

Brault, N., Bourquin, S., Guillocheau, F., Dabard, M.-P., Bonnet, S., Courville, P., Estéoule-Choux, J., and Stepanoff, F.: Mio–Pliocene to Pleistocene paleotopographic evolution of Brittany (France) from a sequence stratigraphic analysis: relative influence of tectonics and climate, Sediment. Geol., 163, 175–210, https://doi.org/10.1016/S0037-0738(03)00193-3, 2004.

Carretier, S., Regard, V., & Soual, C. (2009). Theoretical cosmogenic nuclide concentration in river bed load clasts: Does it depend on clast size?. Quaternary Geochronology, 4(2), 108-123.

Champagnac, J.-D., Molnar, P., Anderson, R. S., Sue, C., and Delacou, B.: Quaternary erosion-induced isostatic rebound in the western Alps, Geology, 35, 195–198, https://doi.org/10.1130/G23053A.1, 2007.

Codilean, A. T., Munack, H., Cohen, T. J., Saktura, W., Gray, A. G., and Mudd, S. M.: OCTOPUS: An open cosmogenic isotope and luminescence database, Earth Syst. Sci. Data, 10, 2123–2139, https://doi.org/10.5194/essd-10-2123-2018, 2018.

Delmas, M., Cerdan, O., Cheviron, B., Mouchel, J.-M., and Eyrolle, F.: Sediment export from French rivers to the sea, Earth Surf. Process. Landf., 37, 754–762, https://doi.org/10.1002/esp.3219, 2012.

Dirks, P. H. G. M., Placzek, C. J., Fink, D., Dosseto, A., and Roberts, E.: Using 10Be cosmogenic isotopes to estimate erosion rates and landscape changes during the Plio-Pleistocene in the Cradle of Humankind, South Africa, J. Hum. Evol., 96, 19–34, https://doi.org/10.1016/j.jhevol.2016.03.002, 2016.

Dunai, T.J., Cosmogenic Nuclides: Principles, Concepts and Applications in the Earth Surface Sciences. Cambridge University Press; https://doi.org/10.1017/CBO9780511804519. 2010.

Dutton, A. and Lambeck, K.: Ice Volume and Sea Level During the Last Interglacial, Science, 337, 216–219, https://doi.org/10.1126/science.1205749, 2012.

Erlanger, E.D., Granger, D.E., and Gibbon, R.J.: Rock uplift rates in South Africa from isochron burial dating of fluvial and marine terraces, Geology, 40, 11, 1019–1022, doi:10.1130/G33172.1.

Gallen, S. F. and Thigpen, J. R.: Lithologic Controls on Focused Erosion and Intraplate Earthquakes in the Eastern Tennessee Seismic Zone, Geophys. Res. Lett., 45, 9569–9578, https://doi.org/10.1029/2018GL079157, 2018.

Granger, D. E., Kirchner, J. W., & Finkel, R. C. (1996). Spatially Averaged Long-Term Erosion Rates Measured from In Situ-Produced Cosmogenic Nuclides in Alluvial Sediment. The Journal of Geology, 104, 249–257.

Guillocheau, F., Brault, Thomas, Barbarand, J., Bonnet, S., Bourquin, S., J, E.-C., Guennoc, P., Menier, D., Néraudeau, D., Proust, J.-N., and Wyns, R.: Histoire géologique du Massif Armoricain depuis 140 Ma (Crétacé-Actuel), Assoc. Géologues Bassin Paris, 40, 13–28, 2003.

Gurnis, M., Mitrovica, J. X., Ritsema, J., and van Heijst, H.-J.: Constraining mantle density structure using geological evidence of surface uplift rates: The case of the African Superplume, Geochem. Geophys. Geosystems, 1, n/a-n/a, https://doi.org/10.1029/1999GC000035, 2000.

Harel, M.-A., Mudd, S. M., and Attal, M.: Global analysis of the stream power law parameters based on worldwide 10Be denudation rates, Geomorphology, 268, 184–196, https://doi.org/10.1016/j.geomorph.2016.05.035, 2016.

Harrison, C. G. A.: What factors control mechanical erosion rates?, Int. J. Earth Sci., 88, 752–763, https://doi.org/10.1007/s005310050303, 2000.

Haxby, W. F. and Turcotte, D. L.: Stresses induced by the addition or removal of overburden and associated thermal effects, Geology, 4, 181, https://doi.org/10.1130/0091-7613, 1976.

Hay, C., Mitrovica, J. X., Gomez, N., Creveling, J. R., Austermann, J., and E. Kopp, R.: The sea-level fingerprints of ice-sheet collapse during interglacial periods, Quat. Sci. Rev., 87, 60–69, https://doi.org/10.1016/j.quascirev.2013.12.022, 2014.

Hurst, M.D., Mudd, S.M., Walcott, R., Attal, M., Yoo, K., 2012. Using hilltop curvature to derive the spatial distribution of erosion rates. Journal of Geophysical Research 117, F02017. https://doi.org/10/f3tx7m

Kaban, M. K., Chen, B., Tesauro, M., Petrunin, A. G., El Khrepy, S., and Al-Arifi, N.: Reconsidering Effective Elastic Thickness Estimates by Incorporating the Effect of Sediments: A Case Study for Europe, Geophys. Res. Lett., 45, 9523–9532, https://doi.org/10.1029/2018GL079732, 2018.

Kirchner, J. W., Finkel, R. C., Riebe, C. S., Granger, D. E., Clayton, J. L., King, J. G., and Megahan, W. F.: Mountain erosion over 10 yr, 10 k.y., and 10 m.y. time scales, Geology, 29, 591, https://doi.org/10.1130/0091-7613(2001)029<0591:MEOYKY>2.0.CO;2, 2001.

Kopp, R. E., Simons, F. J., Mitrovica, J. X., Maloof, A. C., and Oppenheimer, M.: A probabilistic assessment of sea level variations within the last interglacial stage, Geophys. J. Int., 193, 711–716, https://doi.org/10.1093/gji/ggt029, 2013.

Lague, D., Davy, P., and Crave, A.: Estimating uplift rate and erodibility from the area-slope relationship: Examples from Brittany (France) and numerical modelling, Phys. Chem. Earth Part Solid Earth Geod., 25, 543–548, https://doi.org/10.1016/S1464-1895(00)00083-1, 2000.

Lenôtre, N., Thierry, P., Blanchin, R., and Brochard, G.: Current vertical movement demonstrated by comparative levelling in Brittany (northwestern France), Tectonophysics, 301, 333–344, 1999.

Masson, C., Mazzotti, S., Vernant, P., and Doerflinger, E.: Extracting small deformation beyond individual station precision from dense GNSS networks in France and Western Europe, Solid Earth, 10, 1905–1920, https://doi.org/10.5194/se-10-1905-2019, 2019.

Mazzotti, S., Vergeron, X., Malcles, O., Grosset, J., and Vernant, P.: Impact of long-term erosion on crustal stresses and seismicity in stable continental regions, Geology, 51, 733–737, https://doi.org/10.1130/G51327.1, 2023. Monnier Jean Laurent, Jumel Guy, Jumel Alain. Le Paléolithique inférieur de la côte 42 à Saint-Malo-de-Phily (Ille-et-Vilaine). Stratigraphie et industrie. In: Bulletin de la Société préhistorique française, tome 78, n°10-12, 1981. Études et Travaux. pp. 317-328. DOI : https://doi.org/10.3406/bspf.1981.5285

Montgomery, D. R. and Brandon, M. T.: Topographic controls on erosion rates in tectonically active mountain ranges, Earth Planet. Sci. Lett., 201, 481–489, https://doi.org/10.1016/S0012-821X(02)00725-2, 2002.

Muhs, D. R., Pandolfi, J. M., Simmons, K. R., and Schumann, R. R.: Sea-level history of past interglacial periods from uranium-series dating of corals, Curaçao, Leeward Antilles islands, Quat. Res., 78, 157–169, https://doi.org/10.1016/j.yqres.2012.05.008, 2012.

Murray-Wallace, C. M., Belperio, A. P., Cann, J. H., Huntley, D. J., and Prescott, J. R.: Late Quaternary uplift history, Mount Gambier Region, South Australia, Z. Geomorphol., Suppl.-Bd. 106, 41–56, 1996.

Néraudeau, D., Barbe, S., Mercier, D., and Roman, J.: Signatures paléoclimatiques des échinides du Néogène final atlantique à faciès redonien, Ann. Paléontol., 89, 153–170, https://doi.org/10.1016/S0753-3969(03)00023-5, 2003.

Pedoja, K., Husson, L., Regard, V., Cobbold, P. R., Ostanciaux, E., Johnson, M. E., Kershaw, S., Saillard, M., Martinod, J., Furgerot, L., Weill, P., and Delcaillau, B.: Relative sea-level fall since the last interglacial stage: Are coasts uplifting worldwide?, Earth-Sci. Rev., 108, 1–15, https://doi.org/10.1016/j.earscirev.2011.05.002, 2011.

Pedoja, K., Jara-Muñoz, J., De Gelder, G., Robertson, J., Meschis, M., Fernandez-Blanco, D., Nexer, M., Poprawski, Y., Dugué, O., Delcaillau, B., Bessin, P., Benabdelouahed, M., Authemayou, C., Husson, L., Regard, V., Menier, D., and Pinel, B.: Neogene-Quaternary slow coastal uplift of Western Europe through the perspective of sequences of strandlines from the Cotentin Peninsula (Normandy, France), Geomorphology, 303, 338–356, https://doi.org/10.1016/j.geomorph.2017.11.021, 2018.

Peltier, W.R.: Glacial isostatic adjustment: physical models and observational constraints, Rep. Prog. Phys., 85, 096801, 2022.

Polyak, V. J., Onac, B. P., Fornós, J. J., Hay, C., Asmerom, Y., Dorale, J. A., Ginés, J., Tuccimei, P., and Ginés, A.: A highly resolved record of relative sea level in the western Mediterranean Sea during the last interglacial period, Nat. Geosci., 11, 860–864, https://doi.org/10.1038/s41561-018-0222-5, 2018.

Portenga, E. W. and Bierman, P. R.: Understanding Earth's eroding surface with 10Be, GSA Today, 21, 4–10, https://doi.org/10.1130/G111A.1, 2011.

Raymo, M. E. and Mitrovica, J. X.: Collapse of polar ice sheets during the stage 11 interglacial, Nature, 483, 453–456, https://doi.org/10.1038/nature10891, 2012.

Ruszkiczay-Rüdiger, Z., Neuhuber, S., Braucher, R., Lachner, J., Steier, P., Wieser, A., Braun, M., ASTER Team, Bourlès, D., Aumaître, G., and Keddadouche, K.: Comparison and performance of two cosmogenic nuclide sample preparation procedures of in situ produced 10Be and 26Al, J. Radioanal. Nucl. Chem., 329, 1523–1536, https://doi.org/10.1007/s10967-021-07916-4, 2021.

Schaller, M., Von Blanckenburg, F., Veldkamp, A., Tebbens, L. A., Hovius, N., and Kubik, P. W.: A 30 000 yr record of erosion rates from cosmogenic 10Be in Middle European river terraces, Earth Planet. Sci. Lett., 204, 307–320, https://doi.org/10.1016/S0012-821X(02)00951-2, 2002.

Siddall, M., Chappell, J., and Potter, E.-K.: Eustatic sea level during past interglacials, in: Developments in Quaternary Sciences, vol. 7, Elsevier, 75–92, https://doi.org/10.1016/S1571-0866(07)80032-7, 2007.

Steer, P., Simoes, M., Cattin, R., and Shyu, J. B. H.: Erosion influences the seismicity of active thrust faults, Nat. Commun., 5, 5564, https://doi.org/10.1038/ncomms6564, 2014.

Stephenson, R. and Lambeck, K.: Erosion-isostatic rebound models for uplift: an application to south-eastern Australia, Geophys. J. Int., 82, 31–55, https://doi.org/10.1111/j.1365-246X.1985.tb05127.x, 1985.

Stone, J. O.: Air pressure and cosmogenic isotope production, J. Geophys. Res. Solid Earth, 105, 23753–23759, https://doi.org/10.1029/2000JB900181, 2000.

Summerfield, M. A. and Hulton, N. J.: Natural controls of fluvial denudation rates in major world drainage basins, J. Geophys. Res. Solid Earth, 99, 13871–13883, https://doi.org/10.1029/94JB00715, 1994.

Tesauro, M., Kaban, M. K., and Cloetingh, S. A. P. L.: How rigid is Europe's lithosphere?, Geophys. Res. Lett., 36, https://doi.org/10.1029/2009GL039229, 2009.

Toucanne, S., Zaragosi, S., Bourillet, J. F., Cremer, M., Eynaud, F., Van Vliet-Lanoë, B., Penaud, A., Fontanier, C., Turon, J. L., and Cortijo, E.: Timing of massive 'Fleuve Manche' discharges over the last 350kyr: insights into the European ice-sheet oscillations and the European drainage network from MIS 10 to 2, Quat. Sci. Rev., 28, 1238–1256, https://doi.org/10.1016/j.quascirev.2009.01.006, 2009.

Toucanne, S., Zaragosi, S., Bourillet, J.-F., Marieu, V., Cremer, M., Kageyama, M., Van Vliet-Lanoë, B., Eynaud, F., Turon, J.-L., and Gibbard, P. L.: The first estimation of Fleuve Manche palaeoriver discharge during the last deglaciation: Evidence for Fennoscandian ice sheet meltwater flow in the English Channel ca 20–18 ka ago, Earth Planet. Sci. Lett., 290, 459–473, https://doi.org/10.1016/j.epsl.2009.12.050, 2010.

van Dongen, R., Scherler, D., Wittmann, H., & von Blanckenburg, F. (2019). Cosmogenic 10 Be in river sediment: where grain size matters and why. Earth Surface Dynamics, 7(2), 393-410.

Vernant, P., Hivert, F., Chéry, J., Steer, P., Cattin, R., and Rigo, A.: Erosion-induced isostatic rebound triggers extension in low convergent mountain ranges, Geology, 41, 467–470, https://doi.org/10.1130/G33942.1, 2013.

Von Blanckenburg, F.: The control mechanisms of erosion and weathering at basin scale from cosmogenic nuclides in river sediment, Earth Planet. Sci. Lett., 237, 462–479, https://doi.org/10.1016/j.epsl.2005.06.030, 2005.

Westaway, R., Maddy, D., and Bridgland, D.: Flow in the lower continental crust as a mechanism for the Quaternary uplift of south-east England: constraints from the Thames terrace record, Quat. Sci. Rev., 21, 559–603, https://doi.org/10.1016/S0277-3791(01)00040-3, 2002.

Wickert, A. D.: Open-source modular solutions for flexural isostasy: gFlex v1.0, Geosci. Model Dev., 9, 997–1017, https://doi.org/10.5194/gmd-9-997-2016, 2016.